ACS Catalysis

Research Article

pubs.acs.org/acscatalysis

Mechanistic Studies of the Water−Gas Shift Reaction over Pt/$Ce_xZr_{1-x}O_2$ Catalysts: The Effect of Pt Particle Size and Zr Dopant

C. M. Kalamaras,[†] D. D. Dionysiou,[‡] and A. M. Efstathiou*[,†]

[†]Department of Chemistry, Heterogeneous Catalysis Laboratory, University of Cyprus, University Campus, CY 1678, Nicosia, Cyprus

[‡]Department of Civil, Environmental Engineering, University of Cincinnati, Cincinnati, Ohio 45221-0071, United States

Supporting Information

ABSTRACT: A series of *y* wt % Pt/$Ce_xZr_{1-x}O_2$ catalysts (y = 0.1, 0.5, and 1.0; x = 0.3, 0.5, and 0.7) were synthesized and characterized to investigate the effect of CeO_2 doping with Zr^{4+} and of Pt particle size (Pt/$Ce_{0.5}Zr_{0.5}O_2$) on important mechanistic and kinetic aspects of the water−gas shift (WGS) reaction. These included the concentration (μmol·g^{-1} or θ (surface coverage based on Pt_s)) and chemical structure of *active* reaction intermediates present in the "carbon path" and "hydrogen path" of the WGS reaction in the 200−300 °C range and the prevailing mechanism among "redox" and "associative formate" largely considered in the literature. Toward this goal, steady-state isotopic transient kinetic analysis coupled with in situ DRIFTS and mass spectrometry experiments were performed for the first time using D_2O and ^{13}CO isotopic gases. A novel transient isotopic experiment allowed quantification of the initial transient rate of reaction of adsorbed formate (HCOO−) with water and that of adsorbed CO with water under steady-state WGS reaction conditions. On the basis of these results, it was concluded that formate should not be considered as an important intermediate. It was found that on Pt/$Ce_xZr_{1-x}O_2$ catalysts, the WGS reaction mechanism switches from "redox" to a combination of "redox" and "associative formate with −OH group regeneration" mechanisms by increasing the reaction temperature from 200 to 300 °C. The superior WGS activity exhibited by Pt/$Ce_xZr_{1-x}O_2$ (x = 0.3, 0.5, and 0.7) catalysts in comparison with Pt/CeO_2 was explained by the fact that the site reactivity of Pt across the metal−support interface was increased as a consequence of the introduction of Zr^{4+} into the ceria lattice. The concentration of *active* reaction intermediates was found to strongly depend on reaction temperature, support composition (Ce/Zr ratio), and Pt particle size, parameters that all determine the shape of the light-off CO-conversion curve.

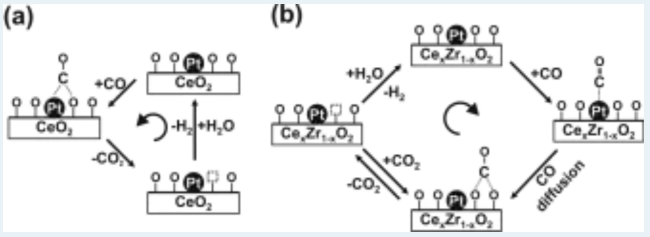

KEYWORDS: *WGS reaction mechanism, ceria−zirconia, SSITKA−DRIFTS, SSITKA−MS, supported Pt, transient isotopic techniques*

1. INTRODUCTION

The concomitant development of a fuel processor in which carbonaceous fuels are converted into hydrogen (H_2) is in increasing demand.[1] The heterogeneously catalyzed water−gas shift (WGS) reaction ($CO + H_2O \leftrightarrow CO_2 + H_2$, $\Delta H^o = -41.2$ kJ/mol) is a key step in a fuel processor and in a number of chemical processes, including steam reforming of hydrocarbons, sugars, alcohols, and bio-oil, which can increase the H_2 concentration in the product gas and at the same time reduce the CO concentration.[2−6]

The low-temperature (180−300 °C) operating industrial $Cu/ZnO/Al_2O_3$ WGS reaction catalyst is pyrophoric and deactivates if exposed to air and condensed water, and it is characterized by low thermal stability.[7,8] Attempts have recently been focused toward the development of low-loading robust noble metal-based catalysts with high activity at low temperatures and that are nonpyrophoric to reduce catalyst volume and cost.[5] Pt metal supported on reducible metal oxide carriers appears to be a promising candidate for replacing current industrial low-temperature WGS catalysts.[6] To increase the intrinsic catalytic activity of supported Pt at low temperatures, various supports, including CeO_2,[5,9−17] ZrO_2,[11−13,17−19] and $Ce_xZr_{1-x}O_2$[13,19−24] have been examined. However, the stability of these catalysts under practical conditions is still problematic and depends on the synthesis method employed.[25] An important aspect in the design of such catalytic systems is the development of a metal oxide support with small grain size, high surface area, controlled porosity, and tailor-designed pore size distribution in an effort to enhance catalytic activity and stability with time on-stream.

Fundamental understanding of the WGS reaction at the molecular level is certainly an important tool toward the design of suitably functional catalytic materials for activity, selectivity, and stability optimization under industrial WGS reaction conditions. To achieve this goal, mechanistic studies of the WGS reaction employing in situ coupled spectroscopic and kinetic measurements under reaction conditions (operando studies) become important.[26,27]

Received: September 20, 2012
Revised: November 4, 2012
Published: November 5, 2012

It is generally accepted that the WGS reaction over metal oxide-supported noble metals operates in a bifunctional manner with the participation of both the dispersed metal and the support phases. In this regard, two general mechanistic schemes have been proposed: (i) The "redox" or "regenerative mechanism",[14,28−34] according to which CO adsorbed on the metal phase is oxidized toward CO_2 by labile oxygen of the support, thus forming an oxygen vacant site. The latter is reoxidized by water, leading to the formation of hydrogen. (ii) The "adsorptive or associative mechanism",[14,15,34−39] according to which the reaction proceeds via the interaction of adsorbed CO with terminal hydroxyl groups (−OH) of the oxidic support to form "carbon-containing" intermediates (e.g., formate, carbonate, or bicarbonate), which are further decomposed toward the formation of gaseous CO_2 and H_2. However, several important kinetic and mechanistic issues of the WGS reaction still remain controversial: (a) the dominant mechanistic pathway, (b) the rate-determining step, and (c) the chemical nature of the active "carbon-containing" and "hydrogen-containing" reaction intermediates and their true site locations (e.g., support alone, metal−support interface, or metal surface).[14,26,40−44]

In the present work, the WGS reaction has been investigated over a series of $Pt/Ce_xZr_{1-x}O_2$ catalysts synthesized by a modified sol−gel technique using surfactant molecules as templates, with emphasis on the influence of Zr^{4+} dopant on essential aspects of the mechanism of the reaction at hand. Toward this goal, steady-state isotopic transient kinetic analysis (SSITKA) coupled with DRIFTS and mass spectrometry experiments have been designed and performed to probe the chemical structure of *active* reaction intermediates and *spectator* species and to estimate the surface concentration of *active* "H-containing" and "C-containing" intermediates found in the "hydrogen path" and "carbon path" of the reaction, respectively. A novel transient isotopic experiment was also performed to quantify the relative importance of the "redox" and "associative formate" WGS reaction mechanisms over the present catalytic systems.

2. EXPERIMENTAL SECTION

2.1. Catalysts Preparation. The $Ce_xZr_{1-x}O_2$ supports were prepared by a modified sol−gel method. The nonionic long-chain surfactant Tween-20 (T20, polyethylene glycol sorbitan monolaurate) was used as a pore-directing agent dissolved in ethanol (EtOH, Fisher). Acetylacetone (Sigma-Aldrich) was then added into the EtOH solution for the esterification reaction, and subsequently, water was added dropwise under vigorous stirring. An appropriate amount of zirconium propoxide (Aldrich) was then added, and the resulting solution was stirred at room temperature for 1 h (zirconia sol). The molar ratio of T20/EtOH/acetylacetone/zirconium propoxide was 1.5/45/6/1 (mol/mol). The appropriate amount of zirconia sol was dissolved in ethanol (Fisher), and the cerium precursor (cerium chloride heptahydrate, Aldrich) was then added under continuous stirring. The molar ratios of Ce/Zr used were 0.3, 0.5, and 0.7. The final sol was transparent and stable for several hours. All preparation steps were conducted at room temperature, and the chemicals were used as received without further purification. The final sol was spread on a glass and dried at 100 °C for 1 h, and the resulting solid product was then calcined in air using a multisegment programmable furnace (Paragon HT-22-D, Thermcraft) at 500 °C at a rate of 18 °C·min^{-1} to remove all the organics. The latter step resulted in the formation of a thick film. The final $Ce_xZ_{1-x}O_2$ (x = 0.3, 0.5, and 0.7) solid was collected by scraping the thick film formed, which was then ground for further characterization and use as a support of Pt.

The supported Pt catalysts were prepared by impregnating the $Ce_xZ_{1-x}O_2$ with a given amount of aqueous solution of $Pt(NH_3)_2(NO_2)_2$ (3.4 wt % solution in NH_4OH, Aldrich) corresponding to the desired Pt loading (0.1, 0.5, and 1.0 wt %). After gradual evaporation of water at 70 °C for 4 h, the resulting slurry was dried at 120 °C overnight and placed in a furnace (ELF 11/6, Carbolite) for calcination in static air at 500 °C for 2 h (heating rate of 50 °C·min^{-1} from 25 to 500 °C). Prior to any catalytic measurements, the fresh sample was pretreated with 20 vol % O_2/He (50 N mL·min^{-1}) at 500 °C for 2 h, followed by reduction in H_2 (1 bar, 50 N mL·min^{-1}) at 300 °C for 2 h.

2.2. Catalyst Characterization. *2.2.1. Textural and X-ray Diffraction Studies.* The $Ce_xZr_{1-x}O_2$ supports were characterized for their texture by the BET method (adsorption of N_2 at 77 K) using a Micromeritics Gemini III surface area and pore size analyzer. The specific surface area ($m^2 \cdot g^{-1}$) of the solid supports was measured after in situ thermal treatment in N_2 gas at 200 °C for 2 h. The primary mean crystallite size of the $Ce_xZr_{1-x}O_2$ solids was estimated on the basis of powder XRD studies (Shimadzu 6000 diffractometer using Cu Kα radiation (λ = 1.5418 Å) and after using the Scherrer formula. The samples had a grain size lower than 200 mesh. X-ray diffractograms were recorded in the 10−80° 2θ range with a step scan of 2°·min^{-1}. In situ XRD studies were performed over the fresh catalyst samples after treatment with a 20 vol % O_2/He (50 N mL·min^{-1}, 2 h) gas mixture in the 200−600 °C range, followed by 20 vol % H_2/He (50 N mL·min^{-1}, 2 h) gas treatment in the 200−600 °C range.

2.2.2. H_2 Temperature-Programmed Desorption (TPD) Studies. The dispersion of Pt metal in the $Pt/Ce_xZr_{1-x}O_2$ (x = 0.3, 0.5, and 0.7) catalysts was determined by selective H_2 chemisorption at 25 °C, followed by temperature-programmed desorption (TPD) in He flow (30 N mL·min^{-1}) using the apparatus and procedures previously described.[45,46] A 0.5-g fresh catalyst sample was first calcined in a 20 vol % O_2/He gas mixture (50 N mL·min^{-1}) at 500 °C for 2 h and then reduced in pure H_2 (30 N mL·min^{-1}) at 300 °C for 2 h. Quantitative analysis of the effluent gas stream from the microreactor was performed using an on line quadrupole mass spectrometer (Omnistar, Balzers) equipped with a fast response inlet capillary/leak valve (SVI050, Balzers) and data acquisition systems. A H/Pt_s = 1 for hydrogen chemisorption stoichiometry was considered. The accuracy of this procedure in determining Pt dispersion for the present $Pt/Ce_xZr_{1-x}O_2$ catalysts was checked by HAADF/STEM measurements described in what follows.

2.2.3. High-Angle Annular Dark Field Scanning Transmission Electron Microscopy. The mean Pt particle size and chemical composition of the 0.5 wt % $Pt/Ce_{0.5}Zr_{0.5}O_2$ solid were estimated using high-angle annular dark field (HAADF) images (200 kV JEM-2100J Jeol Ltd.) obtained from a transmission electron microscope equipped with an INCAx-Sight (Oxford Inc.) energy-dispersive X-ray spectroscopy (EDXS) for elemental chemical analysis. The wt % and atom % compositions of the sample were determined by the provided instrument's software and appropriate calibration procedures. HAADF images were recorded with the microscope in STEM mode with a beam size of 1 nm and an inner collection angle of

68.5 mrad. The contrast in HAADF images is mainly due to differences in the atomic number (Z) of metal elements at constant thickness. Given that $Z_{Pt} = 78$, $Z_{Ce} = 58$, and $Z_{Zr} = 40$, the brighter regions in the HAADF images correspond to Pt particles.

2.2.4. H_2 Temperature-Programmed Reduction (H_2-TPR) Studies. H_2 temperature-programmed reduction (H_2-TPR) experiments were conducted in the gas flow system previously described (section 2.2.2) according to the following procedure. All fresh supported Pt solids were first pretreated in 20 vol % O_2/He gas mixture at 500 °C for 2 h, purged in He flow and then cooled in He to room temperature. A 0.75 vol % H_2/He gas mixture was then passed over the catalyst ($W = 0.1$ g), and the temperature of the solid was increased to 700 °C at a rate of 30 °C·min^{-1}. The mass numbers (m/z) 2, 18, and 32 were used for H_2, H_2O, and O_2, respectively. On the basis of the appropriate material balance, the hydrogen consumption rate (μmol of H_2·g^{-1}·min^{-1}) vs temperature was estimated.

2.2.5. In Situ DRIFTS-CO Chemisorption Studies. A Perkin-Elmer Spectrum GX II FTIR spectrometer equipped with a high-temperature/high-pressure temperature controllable DRIFTS cell (Harrick, Praying Mantis) were used to in situ record infrared spectra obtained under reaction conditions. The spectrum of the solid was taken in Ar flow at the desired reaction temperature, following catalyst pretreatment (20 vol % O_2/Ar at 500 °C for 2 h, followed by pure H_2 at 300 °C for 2 h), and this was subtracted from the spectrum of the solid recorded under the reaction gas mixture at the same temperature. Signal averaging was set to 50 scans per spectrum, and DRIFTS spectra were collected in the 400−4000 cm^{-1} range at a rate of 1 scan·s^{-1} and at a 2 cm^{-1} resolution. DRIFTS spectra when necessary were smoothed to remove high-frequency noise and further analyzed using the software Spectrum in accordance with guidelines reported.[47] CO chemisorption was performed from a 2.98 vol % CO/He gas mixture at 25 °C for 30 min. The DRIFTS flow cell used in the present work was operated in the differential mode (30−35 mg of catalyst sample in fine powder form) without any channelling effects, as previously reported.[14]

2.3. Catalytic Activity Measurements. Steady-state catalytic activity measurements were conducted in the experimental setup previously described in detail.[48] The reaction feed composition used consisted of 3 vol % CO/10 vol % H_2O/87 vol % He, and the total volume flow rate was 200 NmL·min^{-1}, resulting in a GHSV of about 40 000 h^{-1} (L L_{cat}^{-1} h^{-1}). The catalyst particle size was between 0.1 and 0.2 mm, and the amount of catalyst used was 0.5 g. The performance of Pt/$Ce_xZr_{1-x}O_2$ ($x = 0.3$, 0.5, and 0.7) catalysts in terms of CO conversion, X_{CO} (%), vs the reaction temperature (light-off curves), was evaluated in the 200−450 °C range over a prereduced catalyst (H_2/Ar flow at 300 °C for 2 h). After 1 h on reaction stream, where pseudo-steady-state reaction rate was achieved, the catalyst temperature was stepwise increased to the next temperature to be investigated. A stepwise decrease in reaction temperature showed no deactivation of catalyst during the 8 h period of its performance testing. The effluent gas stream from the microreactor after removing the water (Peltier Gas Cooler, model ECP1000, M&C TechGroup) was directed to a mass spectrometer (Omnistar, Balzer) for on line monitoring of the H_2, CO, and CO_2 gases. The purity of all gases used (Linde Gas, Greece; e.g., H_2, He, CO, Ar) was higher than 99.95%.

2.4. Mechanistic Studies. *2.4.1. SSITKA−DRIFTS.* SSITKA−DRIFTS experiments were performed in a specially designed gas flow system, in which the response time of the DRIFTS reactor cell (∼35 mg catalyst) was ∼5 s at the flow rate of 200 NmL·min^{-1}.[14,34,49] Signal averaging was set to 50 scans per spectrum, and the spectra were collected in the 4000−500 cm^{-1} range at the rate of 0.2 scans·s^{-1} (MCT detector) and a resolution of 2 cm^{-1}. The background spectrum of the solid was taken under 10 vol % H_2O/Ar flow at the desired reaction temperature. The DRIFTS data are reported as log (1/R) (absorbance mode) using the relationship, $R = I/I_0$. Here, R is the catalyst sample reflectance, I_0 is the absorbance intensity of the solid itself, and I is the absorbance intensity of both the solid catalyst and the adsorbed species under reaction conditions. The function log (1/R) was found to give a better linear correlation of the integral band against surface coverage than that given by the Kubelka−Munk function for strongly absorbing media.[50] SSITKA−DRIFTS experiments with ^{13}CO (99.9 atom % ^{13}C, Spectra Gases) involved the switch 3 vol % ^{12}CO/10 vol % H_2O/Ar/He (T, 30 min) → 3 vol % ^{13}CO/10 vol % H_2O/Ar (T, t) at a total flow rate of 200 NmL·min^{-1}, which potentially allows determination of the chemical structure of the active intermediate and spectator species of the WGS reaction.

2.4.2. SSITKA−Mass Spectrometry. The isotopes used in the SSITKA−MS experiments were ^{13}CO (99.9 atom % ^{13}C, Spectra Gases) and D_2O (99.96 atom % D, Aldrich). SSITKA experiments were performed using two HPLC pumps (Gilson 307) for the addition of H_2O and D_2O to the reactor feed stream in the apparatus described elsewhere.[48] The SSITKA experiments performed to follow the "hydrogen path" of the WGS reaction involved the switch 3 vol % CO/10 vol % H_2O/Ar/Kr (T, 30 min) → 3 vol % CO/10 vol % D_2O/Ar (T, t), and those to follow the "carbon path" involved the switch 3 vol % ^{12}CO/10 vol % H_2O/Ar/He (T, 30 min) → 3 vol % ^{13}CO/10 vol % H_2O/Ar (T, t). The effluent wet gas stream from the reactor was passed through a condenser (Peltier system of low volume), the exit of which (dry gas) was directed to the mass spectrometer for on line monitoring of the normal and isotope-containing (D, ^{13}C) reactants and products (e.g., H_2, HD, D_2, ^{12}CO, ^{13}CO, $^{12}CO_2$, and $^{13}CO_2$).[45] More details on the SSITKA−MS experiments and the microreactor used were previously reported.[14,27,34,49,51,52] It was estimated that the response time, τ (s), of the system used in SSITKA−MS studies (switching valve → microreactor → condenser → mass spectrometer) was about 5 s on the basis of the transient response curve of Ar to the switch He → 1 vol % Ar/He.[27,51] The mass of the catalyst was adjusted in every SSITKA−MS experiment so as to keep the CO conversion below 15%. The total mass of the catalyst bed was 0.5 g (catalyst diluted with SiO_2).

2.4.3. Steady State WGS Reaction Followed by ^{13}CO Isothermal Isotopic Exchange and Reaction with H_2O. In a recent work,[14] we have presented a novel experiment that allows the measurement of the initial rate of reaction of adsorbed CO and formate species with water alone, in which the surface concentrations of the former species were established under steady-state WGS reaction conditions. The experiment involved the following sequence of steps: 3 vol % ^{12}CO/10 vol % H_2O/Ar (T, 30 min) → 3 vol % ^{13}CO/Ar (T, 5 min) → 10 vol % H_2O/Ar (T, t). The first step aims to replace the adsorbed ^{12}CO with ^{13}CO and leave on the catalyst surface

dx.doi.org/10.1021/cs3006204 | ACS Catal. 2012, 2, 2729−2742

the nonexchangeable $H^{12}COO-$ (formate) species, which were formed under steady-state WGS ($^{12}CO/H_2O/Ar$) reaction conditions. The transient responses of $^{12}CO_2$, $^{13}CO_2$, and H_2 were continuously monitored by an on line mass spectrometer during the 10 vol % H_2O/Ar step. The initial transient rates of $^{12}CO_2$ and $^{13}CO_2$ formation are considered as characteristic rates of the reaction of water with adsorbed $H^{12}COO$-s and $^{13}CO_{ads}$ reaction intermediates and allow discriminating the prevailing mechanism (e.g., "redox" vs "associative formate"). The shape of the $^{12}CO_2$ and $^{13}CO_2$ gas isotopic response curves reflects the kinetics of reaction of adsorbed formate and CO with water, respectively.

3. RESULTS AND DISCUSSION

3.1. Catalyst Characterization. *3.1.1. Solid Support Texture.* The specific surface area, SSA ($m^2 \cdot g^{-1}$), pores volume, V_p ($cm^3 \cdot g^{-1}$), and mean pore diameter, d_p (nm) of the $Ce_xZr_{1-x}O_2$ solid supports are given in Table S1 of the Supporting Information and discussed therein.

3.1.2. Bulk Structure and Composition. X-ray diffraction patterns of fresh $Ce_{0.3}Zr_{0.7}O_2$, $Ce_{0.5}Zr_{0.5}O_2$, $Ce_{0.7}Zr_{0.3}O_2$, and CeO_2 solids are presented in Figure 1a, based on which a single

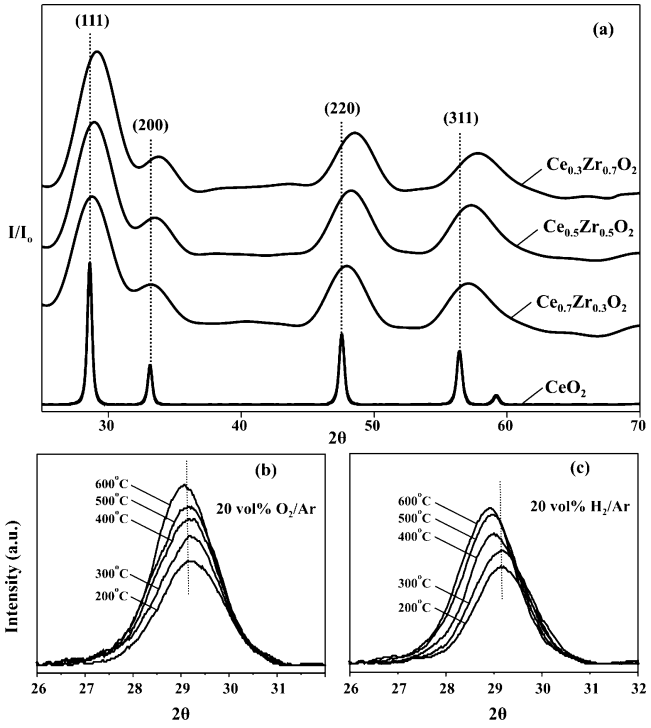

Figure 1. (a) Powder X-ray diffraction patterns of fresh $Ce_xZr_{1-x}O_2$ solids (x = 0.3, 0.5 and 0.7). In situ powder XRD patterns of $Ce_{0.3}Zr_{0.7}O_2$ support after treatment with 20 vol % O_2/Ar (b) and 20 vol % H_2/Ar (c) gas mixtures in the 200−600 °C range.

crystalline phase, that of pseudo-cubic CeO_2−ZrO_2 solid solution, is revealed.[53−57] The diffraction peaks were shifted to higher 2θ values with respect to pure CeO_2 after increasing the Zr content (from x = 0.3 to 0.7), which indicates the shrinkage of the Ce−Zr−O crystal lattice as the result of the introduction of Zr^{4+} into the CeO_2 matrix. This is consistent with the fact that the ionic radius of Zr^{4+} (0.84 Å) is smaller compared with Ce^{4+} (0.97 Å), and as a result of this, the cell parameter, α (Å), of Ce−Zr−O is reduced.[57,58] In fact, the cell parameters of $Ce_{0.7}Zr_{0.3}O_2$, $Ce_{0.5}Zr_{0.5}O_2$, and $Ce_{0.3}Zr_{0.7}O_2$ solid solutions following calcination at 600 °C were found to be 5.3314, 5.3279, and 5.2957 Å, respectively. The introduction of Zr^{4+} was reported to stabilize effectively the CeO_2 matrix against thermal sintering.[58] Figure 1b and c presents XRD patterns of $Ce_{0.3}Zr_{0.7}O_2$ in the 26−32° 2θ range after in situ treatment of the solid with 20 vol % O_2/He and 20 vol % H_2/He, respectively, in the 200−600 °C range (1 h stay at each temperature). The stepwise increase of the temperature under oxidative conditions (20 vol % O_2/Ar) results in an increase in the diffraction peak intensity (Figure 1b), suggesting the formation of a solid with higher crystallinity. On the other hand, under reducing conditions (20 vol % H_2/He, 1 h) the same diffraction peak shifted to lower 2θ values with increasing temperature (Figure 1c), suggesting the expansion of the Ce−Zr−O lattice. This result could be explained by the reduction of Ce^{4+} to Ce^{3+}; the latter ion has a larger ionic radius (1.034 Å) than the former one (0.97 Å).[56,57] Similar XRD patterns were obtained over the $Ce_{0.5}Zr_{0.5}O_2$ and $Ce_{0.7}Zr_{0.3}O_2$ solids. The cell parameter α (Å) of all three solids in their reduced state was increased when compared with that in the oxidized state. For example, after reduction at 300 °C (1 h), the cell parameter of $Ce_{0.7}Zr_{0.3}O_2$, $Ce_{0.5}Zr_{0.5}O_2$, and $Ce_{0.3}Zr_{0.7}O_2$ had values of 5.3786, 5.3713, and 5.3091 Å, respectively. This result indicates the expansion of the crystal lattice due to the fact that fraction of Ce^{4+} was reduced to Ce^{3+}.

Raman studies were also performed on the same $Ce_xZr_{1-x}O_2$ (x = 0.3, 0.5, 0.7) solids to investigate whether single phases of ceria or zirconia were formed, but these could not be detected by powder XRD (d_c < 4.0 nm). The Raman spectra obtained are reported in Figure S1 of the Supporting Information. It is proved that in all three solids, the presence of single-phase CeO_2 or ZrO_2 was absent.

The mean primary crystal size, d_c (nm), of $Ce_xZr_{1-x}O_2$ was estimated after 20 vol % O_2/Ar (500 °C, 2 h) and 20 vol % H_2/Ar (300 °C, 2 h) gas treatments, and the values obtained are reported in Supporting Information Table S1. These pretreatments were the same as those used in the WGS activity measurements over the Pt/$Ce_xZr_{1-x}O_2$ solids. It is seen that d_c is in the 5.7−8.0 nm range, leading to the conclusion that all $Ce_xZr_{1-x}O_2$ solid supports were of nanocrystalline structure.

3.1.3. Platinum Particle Size and Support Chemical Composition. The amount of H_2 desorbed, N_H (μmol $H \cdot g^{-1}$); the platinum dispersion, D (%); and the mean Pt particle size (based on spherical geometry[59]), d_{Pt} (nm), of Pt/$Ce_xZr_{1-x}O_2$ (x = 0.3, 0.5 and 0.7) solids were estimated according to the H_2-TPD procedure (Section 2.2.2). The obtained results are reported in Table S2 of the Supporting Information, and the values of d_{Pt} were compared with those directly obtained from HAADF/STEM measurements (see Supporting Information Figure S2). It is observed that the increase in the Pt loading (from 0.1 to 1.0 wt %) led to a decrease in the Pt dispersion and, thus, to a larger mean Pt particle size. For example, 0.1, 0.5, and 1.0 wt % Pt supported on $Ce_{0.3}Zr_{0.7}O_2$ provided a d_{Pt} of 1.1, 2.1, and 3.3 nm, respectively. HAADF/STEM images provided mean Pt particle sizes within 15−20% accuracy of those reported in Supporting Information Table S2, thus confirming the correctness of the H_2 chemisorption/TPD methodology applied. The elemental analysis of 0.5 wt % Pt/$Ce_{0.5}Zr_{0.5}O_2$ was found to result in 0.48 at. % Ce, 0.51 at. % Zr and 0.47 wt % Pt (EDXS studies), and this catalyst composition was found to be homogeneous across

dx.doi.org/10.1021/cs3006204 | ACS Catal. 2012, 2, 2729−2742

the sample. More details can be found in the Supporting Information.

3.1.4. H_2-TPR (Redox) Studies. Figure 2 shows H_2-TPR traces obtained over the 0.5 and 1.0 wt % $Pt/Ce_{0.5}Zr_{0.5}O_2$ and

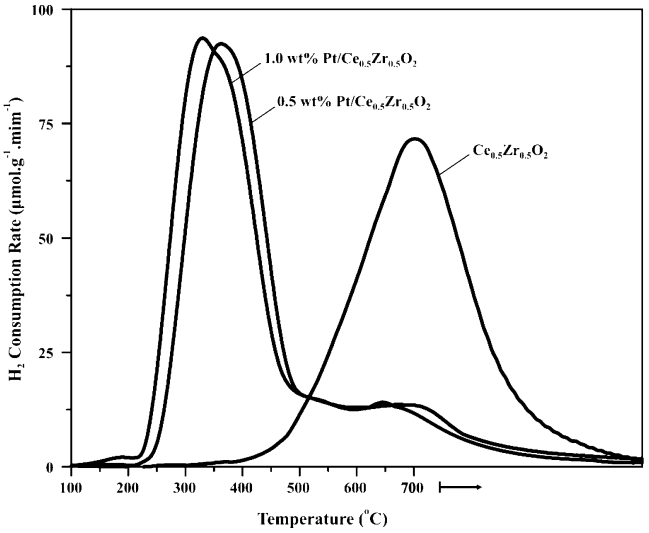

Figure 2. Hydrogen TPR traces obtained over 0.5 wt % $Pt/Ce_{0.5}Zr_{0.5}O_2$, 1.0 wt % $Pt/Ce_{0.5}Zr_{0.5}O_2$, and $Ce_{0.5}Zr_{0.5}O_2$ solid support alone. W = 0.1 g; $Q_{H_2/He}$ = 30 mL·min^{-1}; β = 30 °C·min^{-1}.

the $Ce_{0.5}Zr_{0.5}O_2$ support alone. It is clearly observed that the presence of Pt on the support drastically shifts the H_2-TPR profile of support toward lower reduction temperatures (T_M = 330−360 °C vs 700 °C). In addition, the increase in the Pt particle size shifts the H_2-TPR profile of support further to lower reduction temperatures (compare the H_2-TPR trace of the 1 wt % Pt with that of the 0.5 wt % $Pt/Ce_{0.5}Zr_{0.5}O_2$). The latter result provides a good explanation of the specific WGS activity order observed on these supported-Pt solids, and the followed redox WGS reaction mechanism as is discussed below. Further discussion on the H_2-TPR results of Figure 2 and those obtained on the other $Ce_xZr_{1-x}O_2$- and CeO_2-supported Pt solids can be found in the Supporting Information.

3.1.5. In Situ DRIFTS−CO Chemisorption Studies. Figure 3 presents in situ DRIFTS spectra recorded in the 2150−1800 cm^{-1} range after CO chemisorption at 25 °C for 30 min over

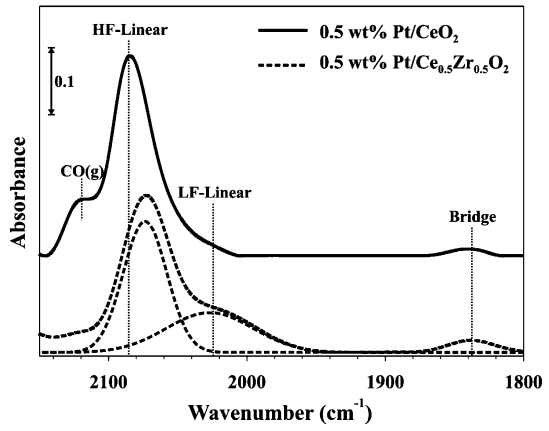

Figure 3. In situ DRIFTS spectra recorded in the 2150−1800 cm^{-1} range following CO chemisorption at 25 °C for 30 min on the 0.5 wt % Pt/CeO_2 (solid line) and 0.5 wt % $Pt/Ce_{0.5}Zr_{0.5}O_2$ catalysts.

the 0.5 wt % $Pt/Ce_{0.5}Zr_{0.5}O_2$ catalyst and after deconvolution and curve-fitting procedures (dashed line). The spectrum obtained over the 0.5 wt % Pt/CeO_2 catalyst[14] is also shown for comparison (solid line). Spectra similar to those reported in Figure 3 were also recorded on $Pt/Ce_{0.3}Zr_{0.7}O_2$ and $Pt/Ce_{0.7}Zr_{0.3}O_2$ catalysts, for which no differences had been observed with regard to the IR band locations.

In the case of Pt/CeO_2, two well-defined infrared bands centered at 2085 and 1838 cm^{-1} were observed, which correspond to high-frequency (HF) linear and bridged adsorbed CO on the Pt surface, respectively.[14,60−70] The IR band of HF linear CO obtained on $Pt/Ce_{0.5}Zr_{0.5}O_2$ is shifted to 2070 cm^{-1}, and a new, smaller in intensity infrared band centered at 2022 cm^{-1} is observed, which is assigned to a low-frequency (LF) linear adsorbed CO on Pt atoms with increased electron density.[20,71] The substantial decrease in the ν(CO) frequency could be explained by the electron transfer from an electron donor species to platinum, which then increases the back-donation of metal electrons into the $2\pi^*$ antibonding orbital of adsorbed CO.[72] Another possible explanation is that after the introduction of Zr^{4+} into the ceria lattice, reduction of the metal oxide ($Ce^{4+} \rightarrow Ce^{3+}$) is facilitated, resulting in the increase in the Ce^{3+} defect site concentration.[19] The latter was proved to be the case on the basis of the H_2-TPR studies presented in Section 3.1.4. According to the discussion above, the LF linear adsorbed CO could be seen as a terminal CO species adsorbed on metallic Pt in contact with reduced Ce^{3+} along the metal−support interface (Pt−□$_s$−Ce^{3+}). The IR band observed at 2120 cm^{-1} corresponds to gas phase CO.[73]

3.2. Catalytic Activity Measurements. Figure 4 reports WGS catalytic activity performance results in terms of CO conversion, X_{CO}(%) vs the reaction temperature (light-off curves) obtained in the 200−375 °C range over the 0.1, 0.5, and 1.0 wt % Pt supported on $Ce_{0.3}Zr_{0.7}O_2$ (a), $Ce_{0.5}Zr_{0.5}O_2$ (b), and $Ce_{0.7}Zr_{0.3}O_2$ (c) solids. The X_{CO} (%)-vs-T curve corresponding to thermodynamic equilibrium, X_{eq} (y^{in}_{CO} = 0.03 and $y^{in}_{H_2O}$ = 0.1) is also given.[52] This curve shows that below 250 °C, full CO conversion can be achieved, and only a minor decrease in X_{CO} by less than 3% units is noticed at 375 °C.

The catalytic activity performance of 0.6 wt % Pt/CeO_2 solid previously reported[14] and that of an industrial LT-WGS catalyst ($CuO/ZnO/Al_2O_3$) measured under the same experimental conditions (W_{cat}, GHSV, feed composition, catalyst particle size) are also depicted in Figure 4. All $Pt/Ce_xZr_{1-x}O_2$ catalysts show higher activity compared with Pt/CeO_2, whereas their activity above 300 °C is higher than that of the industrial LT-WGS catalyst. The significantly higher CO conversions observed on 0.5 wt % $Pt/Ce_xZr_{1-x}O_2$ (x = 0.3, 0.5, and 0.7) compared with 0.6 wt % Pt/CeO_2 in the 200−375 °C range, where all catalysts have similar mean Pt particle size (~1.9−2.4 nm), is an important result, given the fact that Pt/CeO_2 is considered to be one of the most effective catalysts for low-temperature WGS.[28−30,74] Other important characteristics of the catalysts' activity behavior shown in Figure 4 are the following: (a) for a given reaction temperature, there is a monotonic increase of X_{CO} (%) with increasing Pt loading (wt %), independent of support chemical composition (Ce/Zr atom ratio); (b) for the same Pt loading (wt %), variations in X_{CO} (%) with support composition occur mainly at low-temperatures; and (c) for the same support composition, larger variations in X_{CO} (%) with Pt loading occur at low

dx.doi.org/10.1021/cs3006204 | ACS Catal. 2012, 2, 2729−2742

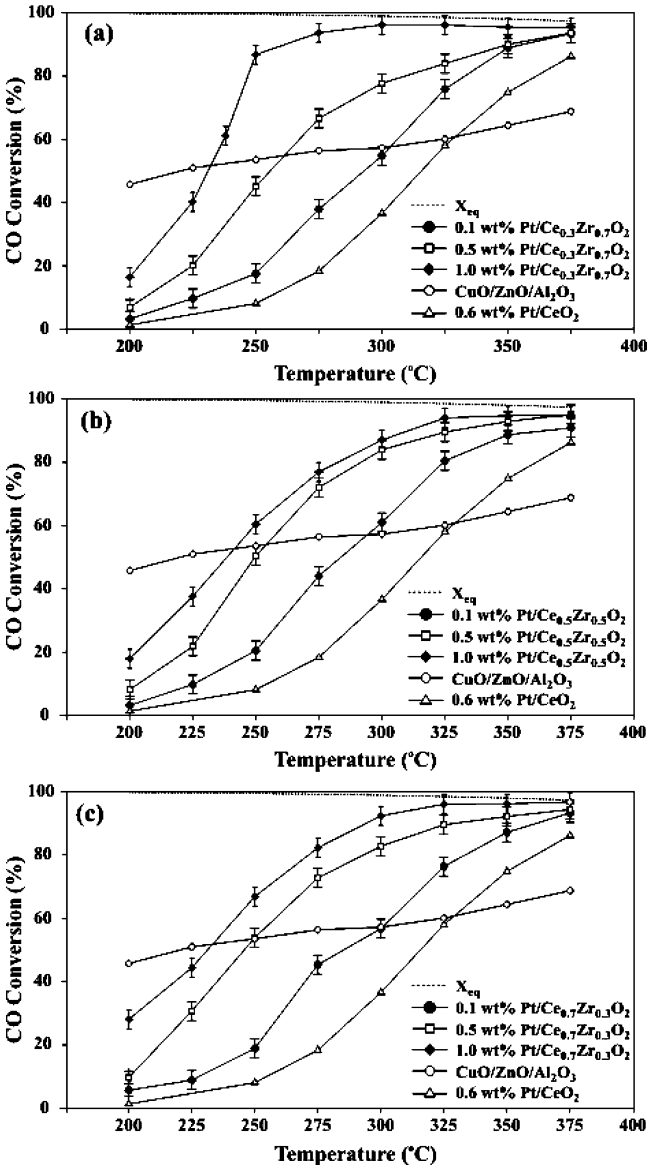

Figure 4. CO conversion (X_{CO}, %) of WGS reaction over x wt % Pt/$Ce_{0.3}Zr_{0.7}O_2$ (a), x wt % Pt/$Ce_{0.5}Zr_{0.5}O_2$ (b), and x wt % Pt/$Ce_{0.7}Zr_{0.3}O_2$ (c) catalysts (x = 0.1, 0.5, and 1.0). The X_{eq} (%)-vs-T profile for equilibrium conditions (y^{in}_{CO} = 0.03 and $y^{in}_{H_2O}$ = 0.1), and that of X_{CO} (%) vs T for the 0.6 wt % Pt/CeO_2 catalyst are also shown. Experimental conditions: W_{cat} = 0.5 g; feed composition: 3 vol % CO, 10 vol % H_2O, He balance gas; total flow rate, Q = 200 NmL/min; GHSV ~ 40 000 h^{-1}.

temperatures. Table S4 (Supporting Information) provides all catalytic activity results shown in Figure 4 for clear reference.

As described in the Introduction, two mechanistic paths have been proposed for WGS reaction: (a) the "redox" and (b) the "associative formate" mechanisms, the extent of each one to depend on catalyst composition and reaction conditions. In the case of the "associative formate" mechanism, key elementary steps are the interaction of adsorbed CO on Pt with terminal −OH groups of partially reduced ceria, forming bridge formates, and their decomposition to CO_2 and H_2.[13,14,39] Thus, the superior WGS activity exhibited by Pt/$Ce_xZr_{1-x}O_2$ in comparison with Pt/CeO_2 could be explained at a first glance by considering that a higher concentration of surface −OH groups is formed on Ce^{3+} defect sites present in Pt/$Ce_xZr_{1-x}O_2$. According to Ricote et al.,[13] addition of Zr^{4+} at the surface of Pt/ceria is expected to lead to the enhancement of $Ce^{3+}-\square_s-Ce^{3+}$ defect sites that are offered for H_2O chemisorption toward −OH groups' generation and the reoxidation of the partially reduced support surface. This, in turn, can lead to the enhancement of formate formation and decomposition rates. This is essentially a two-site model involving both Ce^{3+} and Zr^{4+} surface catalytic sites.

H_2-TPR results reported in Table S3 (Supporting Information) and discussed therein indicate that the reduction extent of $Ce_xZr_{1-x}O_2$ in 0.5 wt % Pt/$Ce_xZr_{1-x}O_2$ was larger than that of CeO_2 in 0.6 wt % Pt/CeO_2. In addition, DRIFTS−CO chemisorption studies (Figure 3) strongly suggested the presence of Ce^{3+} sites at the metal−support interface ($Pt-\square_s-Ce^{3+}$). These results are consistent with theoretical calculations showing that the introduction of zirconium into the ceria lattice decreases the Ce^{4+}/Ce^{3+} reduction energy.[75] In the case of the "redox" mechanism, adsorbed CO on Pt reacts with the partially reducible oxide component at the interface to form CO_2 and at the same time to reduce Ce^{4+} to Ce^{3+}. In this mechanism, reoxidation of oxygen vacancies in ceria by H_2O occurs with H_2(g) formation. It is conceivable, then, that improved surface oxygen mobility could enhance the WGS reaction rate. As will be presented in Section 3.3.4, the "redox" mechanism predominates over that of "associative formate". Therefore, the high WGS activity observed in Pt supported on $Ce_xZr_{1-x}O_2$ could be explained by considering that the introduction of more electronegative Zr than Ce atoms in the ceria lattice induces significant lattice distortions, which increase both the oxygen mobility and the concentration of oxygen vacancies in the lattice,[13,19,21] as evidenced also by the H_2-TPR studies (Figure 2).

Another possible explanation of the high WGS activity of Pt/$Ce_xZr_{1-x}O_2$ solids could be their resistance to the negative effect of CO_2 readsorption, which leads to the formation of various kinds of carbonate species. The sensitivity of noble metals deposited on partially reducible oxides toward CO_2 chemisorption was reported.[9,30,76] As pointed out by Balakos et al.,[77] excellent WGS catalysts in a feed stream that contains no carbon dioxide can exhibit poor activity when appropriate levels of CO_2 are added in the feed stream. Ricote et al.,[13] after a number of gas-switching steps in the feed composition, showed that Pt/ceria−zirconia catalysts are less sensitive to an irreversible deactivation by CO_2 compared with Pt/ceria and Pt/zirconia.

Figure 5 presents the dependence of the intrinsic kinetic rate of WGS at 200 and 300 °C on the mean Pt particle size when the kinetic rate (μmol CO·cm^{-1}·s^{-1}) is based on the length of the perimeter (I_0, cm·g^{-1}) of the Pt−$Ce_{0.5}Zr_{0.5}O_2$ interface. For each catalyst, I_o was estimated considering that for each Pt nanoparticle (hemispherical geometry), a circular geometry for the interface applies.[14] For the three catalysts having 0.1, 0.5, and 1.0 wt % Pt loading, the corresponding Pt mean particle size is 1.7, 2.6, and 8.5 nm (HAADF/STEM studies), which results in I_o equal to 2×10^{10}, 4.1×10^{10}, and 0.78×10^{10} cm·g^{-1}, respectively. Comparing the specific rates of CO conversion at 300 °C for the two catalysts having 1.7 and 8.5 nm mean Pt particle size (3.0×10^{-10} and 3.23×10^{-9} μmol CO·cm^{-1}·s^{-1}, respectively), their ratio is equal to 0.092, whereas the corresponding ratio of their I_o values is 2.56. Thus, it is rather clear that the large difference in the specific rates of the two catalysts is not due to the different I_o values. Considering the fact that the number density (atoms/cm) of Pt

dx.doi.org/10.1021/cs3006204 | ACS Catal. 2012, 2, 2729−2742

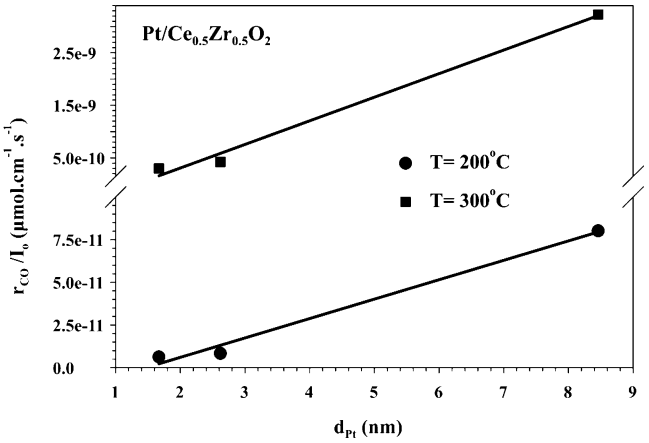

Figure 5. Effect of Pt mean particle size, d_{Pt}, on the specific rate of CO conversion based on the perimeter of the Pt–support interface (μmol CO·cm^{-1}·s^{-1}) for the WGS reaction at 200 and 300 °C performed on the Pt/$Ce_{0.5}Zr_{0.5}O_2$ catalyst.

along the interface should be considered rather constant with Pt particle size, then the specific rate of CO conversion expressed per Pt atom present along the metal–support interface should also follow the same linear relationship shown in Figure 5. This important result suggests that the intrinsic site reactivity of Pt atoms along the metal–support interface is different, depending on the Pt particle size, as first reported in the case of the Pt/CeO_2 catalyst.[14] As will be shown in Section 3.3, the "redox" mechanism applies to the present catalytic system in the 200–300 °C range, where Pt and oxygen atoms at the metal–support interface are considered as active catalytic sites. Therefore, the above offered kinetic analysis should be considered as more appropriate than that based on TOF (s^{-1}), the latter taking into account active catalytic sites present only on the Pt surface. The H_2-TPR results of Figure 2 support the specific kinetic rate results of WGS presented in Figure 5. As the Pt particle size increases, lattice oxygen mobility in the vicinity of Pt nanoparticles increases; thus, the shift of reduction rate-vs-*T* profile toward lower temperatures seen in Figure 2.

3.3. Mechanistic Studies. *3.3.1. SSITKA–DRIFTS.* In situ DRIFTS spectra recorded in the 3050–1200 cm^{-1} range on the 0.5 wt % Pt/$Ce_{0.5}Zr_{0.5}O_2$ catalyst during SSITKA–DRIFTS experiments (Section 2.4.1) at 200 °C are presented in Figure 6a–c. The 2250–1850 cm^{-1} range (Figure 6a) corresponds to linear adsorbed CO on Pt;[14,15,20,34,71,78–81] that of 1700–1200 cm^{-1} (Figure 6b), to the O–C–O stretching vibrational modes of formate, carbonate, and carboxylate species;[11,13,36,74,79,82–84] and that of 3050–2650 cm^{-1} (Figure 6c), to formate (HCOO–) species (νCH, δCH + νOCO_{as} and δCH + νOCO_s vibrational modes).[11,13–15,34,36,79,83–88] Deconvoluted and curve-fitted spectra obtained under both $^{12}CO/H_2O$ and $^{13}CO/H_2O$ reaction feed streams are also shown (Figure 6a, b). All spectra recorded under $^{12}CO/H_2O$ steady-state reaction conditions (30 min on-stream) are presented by a solid line, whereas the deconvoluted and curve-fitted ones corresponding to the $^{13}CO/H_2O$ steady state are presented by a dashed line (bottom graph).

The intense IR band centered at 2037 cm^{-1} (Figure 6a, band 3) is due to a HF linear adsorbed CO on Pt. The broad IR band (2090–1890 cm^{-1}) located at 2000 cm^{-1} (band 4) is assigned to a LF linear adsorbed CO on Pt atoms along the metal–

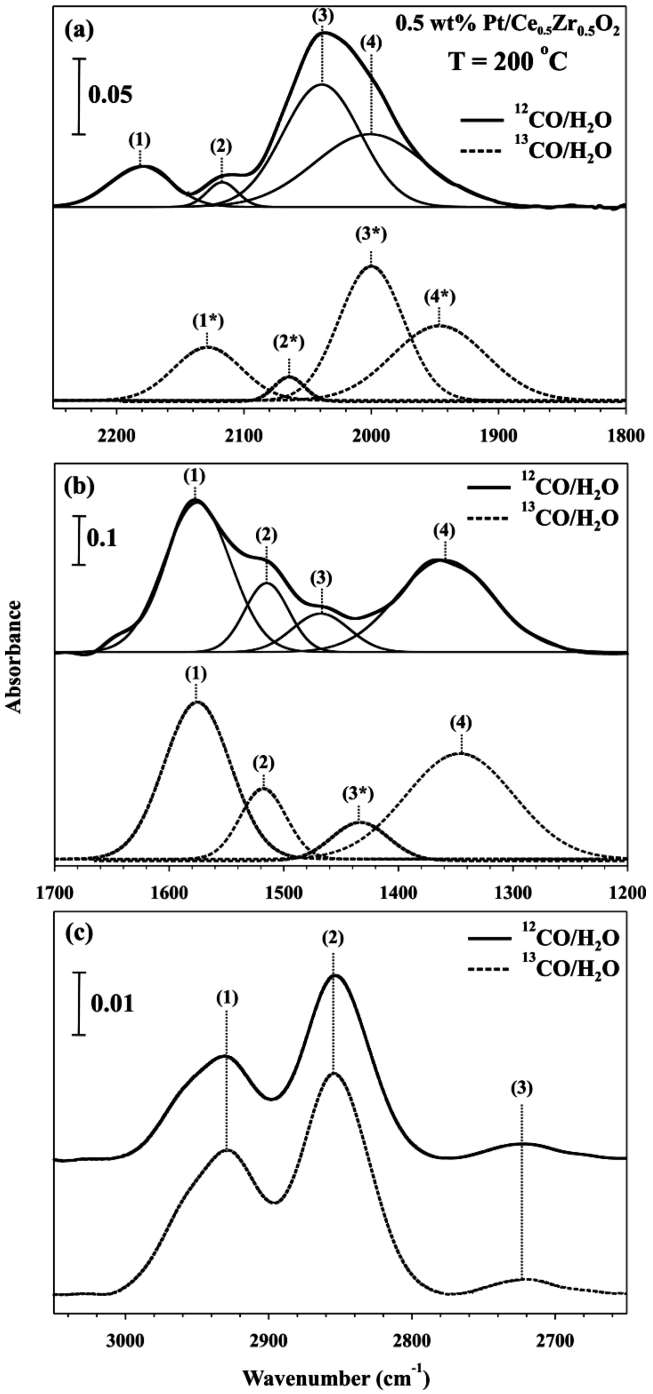

Figure 6. In situ DRIFTS spectra recorded in the range of (a) 2250–1800, (b) 1700–1200, and (c) 3050–2650 cm^{-1} over 0.5 wt % Pt/$Ce_{0.5}Zr_{0.5}O_2$ during SSITKA–WGS reaction at 200 °C in 3 vol % ^{12}CO/10 vol % H_2O/Ar (solid spectra), and 3 vol % ^{13}CO/10 vol % H_2O/Ar (dashed spectra) feed gas mixtures. Deconvolution and curve-fitting of recorded IR spectra are also shown.

support interface, as discussed in Section 3.1.5. The IR bands centered at 2179 and 2117 cm^{-1}, labeled as 1 and 2, respectively, are due to gas phase ^{12}CO.[73] As depicted in Figure 6a (bottom graphs), all the IR bands described above show the red isotopic shift upon the switch $^{12}CO/H_2O \rightarrow {}^{13}CO/H_2O$, and these are labeled with an asterisk (*). On the basis of only the observed red isotopic shift, it is not safe to conclude that all these species are necessarily active reaction

dx.doi.org/10.1021/cs3006204 | ACS Catal. 2012, 2, 2729–2742

intermediates, since reversible adsorption of CO on Pt (exchange process), $^{12}CO_{ads} + {}^{13}CO_{gas} \leftrightarrow {}^{13}CO_{ads} + {}^{12}CO_{gas}$, can give rise to the red isotopic shift. On the other hand, in agreement with our previous studies,[14,15,34,49] at least one kind of adsorbed CO on Pt must be considered as an active intermediate of the "carbon path" of the WGS reaction, since CO is the only "C-containing" reactant species.

The IR bands recorded at 1576 (Figure 6b, band 1) and 1362 cm^{-1} (Figure 6b, band 4) under the $^{12}CO/H_2O$ gas mixture are due to the OCO_{as} and OCO_s vibrational modes of formate (HCOO−), whereas those centered at 1515 (Figure 6b, band 2) and 1468 cm^{-1} (Figure 6b, band 3) are due to carboxylates and unidentate carbonates, respectively. The IR bands centered at 2931, 2852, and 2721 cm^{-1} (Figure 6c, solid line spectrum) are due to the νCH, δCH + νOCO_{as}, and δCH + νOCO_s vibrational modes of adsorbed HCOO− on the support.[11,13−15,36,74,79,82−84] After the new steady state under the isotopic $^{13}CO/H_2O$ gas mixture was reached, it was seen that only the IR band labeled as 3* due to carbonate species showed the red isotopic shift (Figure 6b). This result is related either to CO_2 readsorption effects, in which part of the carbonate species formed under WGS is reversibly chemisorbed, or to carbonates that could be considered as true active reaction intermediates based on a "redox" mechanism, as will be discussed below. On the other hand, it is clear that formate and carboxylate species formed on the $Ce_xZr_{1-x}O_2$ support surface at 200 °C must be considered as *inactive* species, since their characteristic IR bands (νCH and OCO vibrational modes) did not give the red isotopic shift (Figure 6b−c).

Figure 7a−c shows similar SSITKA−DRIFTS spectra recorded on the 0.5 wt % $Pt/Ce_{0.5}Zr_{0.5}O_2$ catalyst at 300 °C. It is observed that the IR band 4 (Figure 7a, 1996 cm^{-1}) related to the LF linear adsorbed CO on Pt in contact with Ce^{3+} defect sites presents an increased integral absorbance compared with that obtained at 200 °C ($I_{(4)}^{300\ °C}/I_{(4)}^{200\ °C}$ = 1.62). The opposite was found with the HF linear adsorbed CO (band 3, Figure 7a, 2050 cm^{-1}; $I_{(3)}^{300\ °C}/I_{(3)}^{200\ °C}$ = 0.50). All IR bands related to adsorbed CO on Pt gave the red isotopic shift (Figure 7a) as has also been observed at 200 °C (Figure 6a). The characteristic IR bands of formate and carbonate species on the support were also observed at 300 °C (Figure 7b−c). Nevertheless, the deconvolution and curve-fitting procedures of the spectra recorded under the $^{13}CO/H_2O$ gas treatment (Figure 7b−c, dashed line) provided the red isotopic shift for all bands, a result opposite of that obtained at 200 °C. The latter suggests that in the case of $Pt/Ce_{0.5}Zr_{0.5}O_2$, the formate species formed on the support surface appears to switch from being an *active* intermediate at 300 °C to an *inactive* species at 200 °C. It is apparent that the chemical composition of the active reaction intermediates found in the "carbon path" of WGS depends on reaction temperature. This behavior is in harmony with our previous studies[15] on Pt/CeO_2 and those reported by Meunier et al.[89,90] In the latter work, formates were considered as *inactive* species at T < 160 °C but *active* reaction intermediates at T > 220 °C. As previously mentioned, the existence of a red isotopic shift cannot be considered by itself as a safe criterion to judge whether the related adsorbed species can be considered as active reaction intermediates. Thus, even though formates (Figure 7b−c) on the support had given the red isotopic shift at 300 °C, these species may not be *important active* reaction intermediates, according to what is presented next.

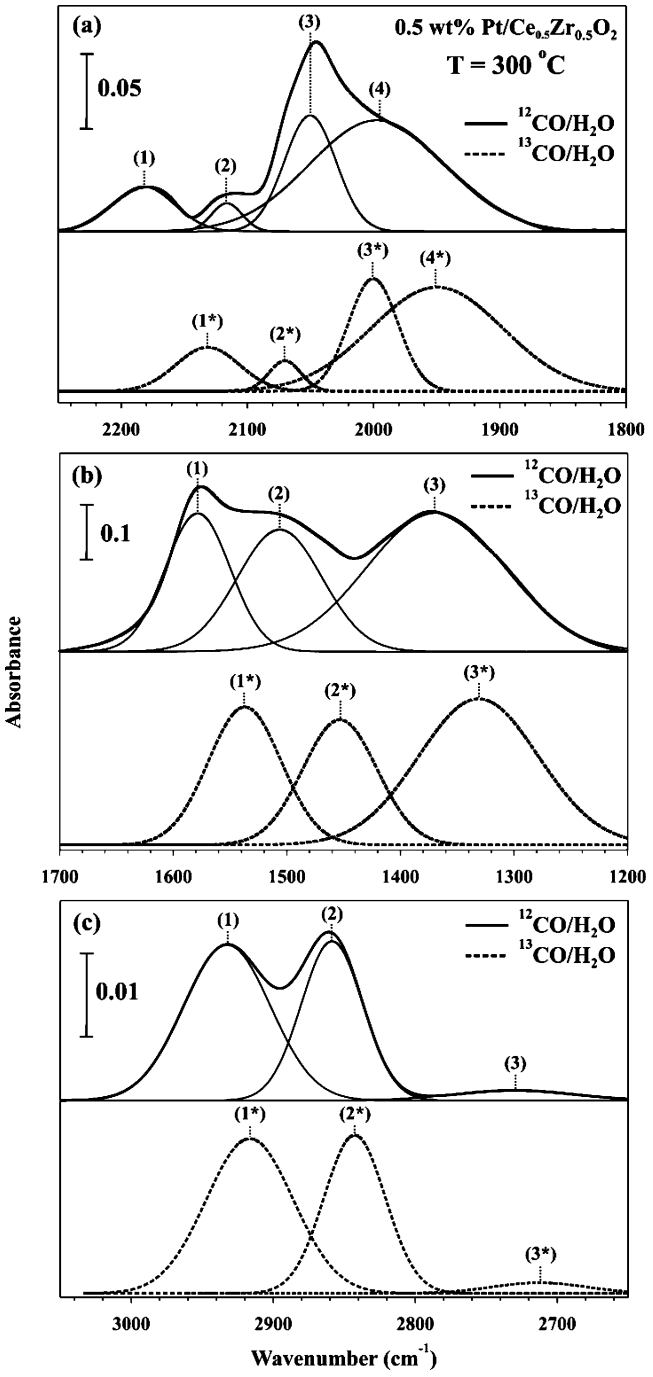

Figure 7. In situ DRIFTS spectra recorded in the range of (a) 2250−1800, (b) 1700−1200, and (c) 3050−2650 cm^{-1} over 0.5 wt % $Pt/Ce_{0.5}Zr_{0.5}O_2$ during the SSITKA−WGS reaction at 300 °C in 3 vol % ^{12}CO/10 vol % H_2O/Ar (solid spectra) and 3 vol % ^{13}CO/10 vol % H_2O/Ar (dashed spectra) feed gas mixtures. Deconvolution and curve-fitting of recorded IR spectra are also shown.

3.3.2. SSITKA−Mass Spectrometry. SSITKA−mass spectrometry (MS) experiments were used to quantify the "hydrogen path" and "carbon path" of the WGS reaction mechanism(s) from H_2O and CO reactants to H_2 and CO_2 gas products at 200 and 300 °C under a kinetic regime (X_{CO} < 20%). Figure 8a presents transient concentration response curves of H_2, HD, D_2, and Kr obtained after the isotopic switch $CO/H_2O/Ar/Kr \rightarrow CO/D_2O/Ar$ was made over the 0.5 wt % $Pt/Ce_{0.5}Zr_{0.5}O_2$ catalyst at 300 °C. The concentration

dx.doi.org/10.1021/cs3006204 | ACS Catal. 2012, 2, 2729−2742

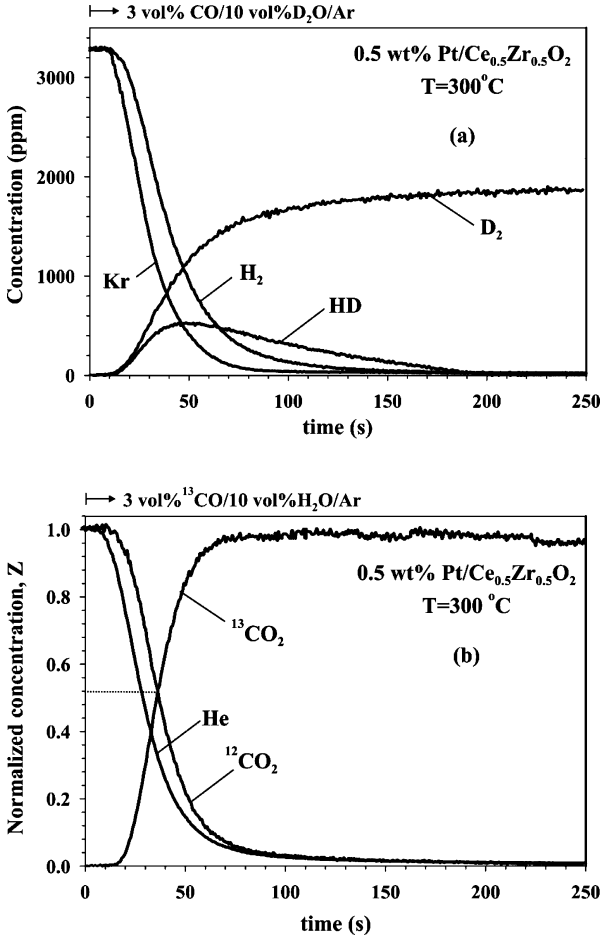

Figure 8. SSITKA–mass spectrometry experiments performed to estimate the *active* "hydrogen-containing" (H-pool) (a) and the *active* "carbon-containing" (C-pool) (b) reaction intermediates found in the WGS reaction paths on 0.5 wt % $Pt/Ce_{0.5}Zr_{0.5}O_2$ catalyst at 300 °C. Gas delivery sequence: (a) 3 vol % CO/10 vol % H_2O/Ar/Kr (30 min) → 3 vol % CO/10 vol % D_2O/Ar (t); (b) 3 vol % ^{12}CO/10 vol % H_2O/Ar/He (30 min) → 3 vol % ^{13}CO/10 vol % H_2O/Ar (t).

(μmol·g^{-1}) of active "H-containing" intermediates, named "H-pool", is estimated on the basis of the transient response curves of H_2, HD, and Kr as described elsewhere,[14,34,49,52] and the obtained results are given in Table 1 for the x wt % $Pt/Ce_{0.5}Zr_{0.5}O_2$ (x = 0.1, 0.5, and 1.0) catalysts. For critical comparison, corresponding results for the Pt/CeO_2 catalytic system[14,15] are also given in Table 1. The equivalent amount of "H-pool" in terms of surface Pt monolayers (θ) is also provided in Table 1 (numbers in parentheses).

The formation of HD(g) might be the result of the recombination of adsorbed H and D on the Pt surface and the exchange of the H of the −OH group of the support with the D from the D_2(g) and/or D_2O(g) under the $^{12}CO/D_2O$/Ar gas switch, leading to an overestimation of the "H-pool". This was carefully checked according to our previous works,[15,34] and it was found to be insignificant. On the other hand, it should be pointed out that the reversibly adsorbed H or D on the Pt surface is included in the estimation of "H-pool" because H_2(g) on Pt is expected to be formed by the recombination of two adjacent adsorbed H species; the adsorbed H on Pt is considered as a true *active* reaction intermediate.

It is seen from Table 1 that the surface coverage of the active "H-pool" is in the range of $2.0 < \theta_H < 5.8$ and $68.5 < \theta_H < 125.3$

Table 1. Concentration (μmol·g^{-1}) and Surface Coverage (θ)[a] of Active "Hydrogen-Containing" (H-pool) and "Carbon-Containing" (C-pool)[b] Species Found in the Mechanism of the WGS Reaction at 200 and 300 °C over x wt % $Pt/Ce_{0.5}Zr_{0.5}O_2$ Catalysts (x = 0.1, 0.5 and 1.0) Measured by SSITKA–MS Experiments

	C-pool[b] (μmol·g$_{cat}^{-1}$) or θ_C		H-pool (μmol·g$_{cat}^{-1}$) or θ_H	
catalyst	200 °C	300 °C	200 °C	300 °C
0.1 wt % $Pt/Ce_{0.5}Zr_{0.5}O_2$	11 (3.2)[a]	46 (13.6)[a]	7 (2.0)[a]	232 (68.5)[a]
0.5 wt % $Pt/Ce_{0.5}Zr_{0.5}O_2$	25 (2.4)	109 (10.3)	31 (2.9)	719 (67.9)
1.0 wt % $Pt/Ce_{0.5}Zr_{0.5}O_2$	32 (4.7)	149 (22.4)	39 (5.8)	835 (125.3)
0.6 wt % Pt/CeO_2[c]		1.9 (0.17)		8.6 (0.75)
0.5 wt % Pt/CeO_2[d]	12.9 (0.9)	61.7 (4.5)	77 (5.6)	2816 (204)

[a]In terms of surface monolayers of platinum (based on HAADF/STEM studies). [b]Corrected values from CO_2 readsorption effects (see Figure 9 and Section 3.3.3). [c]Adopted from ref 14. [d]Adopted from ref 15.

when the WGS reaction is performed at 200 and 300 °C, respectively, on x wt % $Pt/Ce_{0.5}Zr_{0.5}O_2$ solids. This result strongly suggests that these "H-containing" species largely reside on the surface of $Ce_{0.5}Zr_{0.5}O_2$ support. The chemical nature of these active intermediates is considered to be labile hydroxyls (−OH) and atomic hydrogen (H), both produced via water dissociation. Atomic hydrogen species should be regarded as attached on a surface oxygen anion, O^{n-} of the $Ce_{0.5}Zr_{0.5}O_2$ support. It has been suggested[11,12,34,91] that oxygen vacancies (Ce^{3+}–□$_s$–Ce^{3+}) in partially reducible metal oxides (e.g., CeO_2, TiO_2) can act as specific sites for H_2 activation. Evidence for the presence of such sites at the metal–support interface ([Pt–□$_s$–Ce^{3+}] site) is provided by the appearance of the LF linear adsorbed CO band (2022 cm^{-1}, Figure 3), as previously discussed. Formate species (HCOO−) could also be considered as active "H-containing" intermediates; However, on the basis of the SSITKA–DRIFTS studies (Section 3.3.1) and other transient isotopic experiments performed at 200 °C, which are presented below, formate species residing on the support should be considered as *inactive* (spectator) species. In the case of 0.5 wt % Pt/CeO_2 catalyst,[15] the H-pool at 200 °C is about twice as large as that of 0.5 wt % $Pt/Ce_{0.5}Zr_{0.5}O_2$. Given the fact that the two catalytic systems have similar mean Pt particle sizes, it is implied that the size of the reactive zone around each Pt nanoparticle in Pt/CeO_2 must be twice as large as in the $Pt/Ce_{0.5}Zr_{0.5}O_2$ catalyst. By determining the total specific perimeter (cm·g$_{cat}^{-1}$) of supported Pt particles (assuming hemispherical geometry), as previously discussed (Figure 5) and reported,[14] and considering a distance between two adjacent −OH groups of about 2 Å, the concentration of −OH groups present along the periphery of the metal–support interface can be estimated. The latter was found to be in the range of 0.6–3.3 μmol·g$_{cat}^{-1}$ for the present x wt % $Pt/Ce_{0.5}Zr_{0.5}O_2$ catalysts. These values are smaller than the ones reported for the size of the active "H-pool" (Table 1), clearly suggesting that there is a *reactive zone* around each Pt nanoparticle within which active OH/H species are formed and participate in the "H path" of WGS reaction. The results shown in Table 1 find support from previous studies on Pt/γ-Al_2O_3,[49,52] Au/CeO_2,[43,92] Pt/TiO_2,[15,34] and Pt/CeO_2[14,15]

dx.doi.org/10.1021/cs3006204 | ACS Catal. 2012, 2, 2729–2742

catalysts, in which the presence of a *reactive zone* around the metal nanoparticles under steady-state WGS reaction conditions is established.

The effect of support chemical composition (Ce/Zr atom ratio) on the kinetic rate of WGS and, in turn, on the activity results shown in Figure 4 can be understood on the basis of a kinetic analysis similar to that previously discussed for the effect of Pt particle size (Figure 5). At 300 °C, the specific kinetic rate r_{CO}/I_o (μmol·cm^{-1}·s^{-1}) of WGS for the present 0.5 wt % Pt/$Ce_{0.5}Zr_{0.5}O_2$, 0.5 wt % Pt/CeO_2[15], and 0.6 wt % Pt/CeO_2[14] catalysts (all having a similar Pt mean particle size, $d_{Pt} \sim 2.0$ nm) is 4.95×10^{-10}, 2.3×10^{-10}, and 0.75×10^{-10} μmol·cm^{-1}·s^{-1}. These results clearly illustrate that the Pt site reactivity (k, s^{-1}) along the Pt−support interface is different for the three catalysts. It is suggested that when Pt nanoparticles are deposited on the $Ce_{0.5}Zr_{0.5}O_2$ support, active sites of larger reactivity than when Pt is deposited on CeO_2 along the Pt−support interface and around each Pt nanoparticle are formed for CO chemisorption, water dissociation (OH formation), and activation of lattice oxygen. A significant result is the fact that among the two ceria supports investigated, the specific kinetic rate, r_{CO}/I_o (μmol·cm^{-1}·s^{-1}), differs by a factor of 3. This result largely supports the findings of Panagiotopoulou et al.[93] regarding the effect of the particle size of the support (d_c, nm) on the specific kinetic rate of WGS for the Pt/TiO_2 catalytic system.

On the basis of the SSITKA results reported in Figure 8a, the rate of H_2 formation under $^{12}CO/H_2O/Ar$ is lower by a factor of 1.8 compared with the rate of D_2 formation under the $^{12}CO/D_2O/Ar$ feed gas stream. The latter result implies the existence of a normal kinetic isotopic effect (NKIE). The NKIE is related to the strength of the chemical bond(s) involved in the rate-determining step (RDS) of the reaction. For the present WGS reaction, one of the following steps could be considered as the RDS: (i) water dissociation on the support ("redox" mechanism), (ii) formate (HCOO−) decomposition ("associative" mechanism), (iii) surface diffusion of H/OH species (breaking of O−H bonds), and (iv) recombination of two adjacent adsorbed H species on Pt to form H_2(g). A normal kinetic isotopic effect was also reported for other supported Pt catalysts.[15,34,39,52,94,95] Ricote et al.[13] proposed that the rate-determining step could be that of formate decomposition on Pt. On the basis of the present SSITKA−DRIFTS studies (Section 3.3.1), formates cannot be considered as true active reaction intermediates at 200 °C. It was reported that water promotes the rate of WGS on Pt/CeO_2[57] by the formation of −OH groups adjacent to the formate active intermediate; thus, a reactant-promoted mechanism was proposed. Water dissociation on oxygen vacant sites or abstraction of surface lattice oxygen related to the "redox" mechanism might be considered as a likely RDS in the case of WGS at 200 °C on the present x wt % Pt/$Ce_{0.5}Zr_{0.5}O_2$ catalysts (x = 0.1, 0.5, and 1.0).

Figure 8b shows normalized dynamic response curves (Z) of $^{12}CO_2$, $^{13}CO_2$, and He obtained after the isotopic switch $^{12}CO/H_2O/Ar/He \rightarrow {}^{13}CO/H_2O/Ar$ at 300 °C was made over the 0.5 wt % Pt/$Ce_{0.5}Zr_{0.5}O_2$ catalyst. An exponential-like decay of the $^{12}CO_2$ dimensionless concentration response curve accompanied by a mirrorlike growth of the corresponding $^{13}CO_2$ one was observed, in which both curves cross each other at Z = 0.515 instead of 0.5 (~3% experimental error) according to the SSITKA theory.[23,24,27,50] The concentration and surface coverage (θ) of active "carbon-containing" intermediates, named "C-pool", which are found in the "carbon path" of the WGS reaction, were estimated on the basis of the $^{12}CO_2$ and He response curves and a material balance equation described elsewhere.[14,34,49,52] The obtained results are given in Table 1. No ^{13}C-isotopic kinetic effect was observed because the steady-state rates of $^{12}CO_2$ and $^{13}CO_2$ under the nonisotopic and isotopic CO/H_2O gas mixtures were the same.

The concentration (μmol·g^{-1}) and surface coverage (θ) reported in Table 1 refer to all "C-containing" active reaction intermediates formed during steady-state WGS and which led to CO_2(g) formation; namely, adsorbed CO (CO_{ads}) on Pt, carbonates CO_3^{2-}, and/or formates (HCOO−) on the support. It is important to point out that the $^{12}CO_2$(g) and $^{13}CO_2$(g) response curves are influenced by CO_2 readsorption effects on both active and nonactive catalytic sites.[27,50] This effect was carefully considered, as will be discussed in the following section. Thus, the values of the concentration of the "C-pool" reported in Table 1 are true values free of CO_2 readsorption effects. On the basis of the "C-pool", in terms of θ_C, which are in the 2.4−22.4 range for all three Pt/$Ce_{0.5}Zr_{0.5}O_2$ catalysts at 200 and 300 °C, it is shown that a large part of the active "C-containing" intermediates are formed along the Pt−support interface and within a reactive zone around each Pt nanoparticle, a result that is also supported by the analysis of kinetic rate data as a function of Pt particle size, previously presented (Figure 5) and discussed. It is important to note that the surface coverage of "C-containing" intermediates formed on Pt/$Ce_{0.5}Zr_{0.5}O_2$ at 300 °C ($10.3 < \theta_C < 22.4$) is found to be significantly larger compared with that found in our previous work on a series of Pt/CeO_2 catalysts ($0.03 < \theta_C < 0.17$, Table 1). This result illustrates that the addition of Zr^{4+} into the ceria lattice leads to significant enhancement of the surface concentration of active intermediates within the reactive zone and which are involved in the "carbon path" of WGS. This, in turn, provides a good explanation for the observed enhanced activity exhibited by the present Pt/$Ce_xZr_{1-x}O_2$ solids compared with Pt/CeO_2, in addition to the site reactivity (k, s^{-1}), as discussed above.

The catalytic activity behavior shown in Figure 4 is well connected with the intrinsic kinetic rate applied for each catalytic system. As previously discussed to a great extent, the support chemical composition and the Pt particle size strongly influence the specific reaction rate expressed per length of the perimeter of Pt−support interface (μmol CO·cm^{-1}·s^{-1}). The latter kinetic parameter is the most appropriate to understand the results of Figure 4 after having proved the participation of support in the "redox" mechanism of WGS applied here. According to the results of Table 1, the surface concentration of active species leading to H_2 and CO_2 depends strongly on the support chemical composition, the Pt particle size, and the reaction temperature. These kinetic parameters are established under steady-state reaction conditions as the result of the influence of the site reactivity (k, s^{-1}) of the species involved in the rate-determining step. The latter is influenced, in turn, by the reaction temperature through the Arrhenius relationship ($k = k_0\exp(-E/RT)$). The S-shape-like curve of the X_{CO} (%)-vs-T profile is basically the result of the effect of k and the surface concentration of the active species (Table 1) within the reactive zone on the rate of the reaction. As the reaction temperature increases, it was shown (see also Section 3.3.4) that the "associative formate" mechanism starts to operate in parallel to "redox" but to a small extent up to 300 °C. Thus, it would be reasonable to suggest that the extent of participation of each

dx.doi.org/10.1021/cs3006204 | ACS Catal. 2012, 2, 2729−2742

mechanism in the WGS also determines the quality of the S-shape curve of the X_{CO} (%)-vs-T profile shown in Figure 4.

According to the proposed mechanistic paths of the WGS reaction,[11,14,15,29,34,49,52,83,93] it is possible for adsorbed CO on Pt (Pt−CO_s) to follow two routes: (i) reversible interaction with −OH groups on the support to form formate (HCOO−) species, which in turn decompose to CO_2(g) and atomic hydrogen (H-s), and (ii) direct reaction with the support surface lattice oxygen to form carbonate species, CO_3^{2-}, the latter decomposing into gaseous CO_2 according to the following elementary reaction steps:

$$CO_s + OH-_L \leftrightarrow HCOO-_L + s \rightarrow CO_2(g) + H - s + \square_L \quad (1)$$

$$CO_s + 2[O-_L]^{n-} \rightarrow [CO_3]^{n-} -_L + s \quad (2)$$

$$[CO_3]^{n-} -_L \leftrightarrow CO_2(g) + (O-_L + \square_L)^{n-} \quad (3)$$

where, $\square_L$ is a surface oxygen vacant site in the support, s is a Pt surface site, and L is a support surface site.

According to Figure 6b, where only carbonate species provided the red isotopic shift, reaction steps 2 and 3 comprise part of the sequence of steps found in the "C path" of WGS at 200 °C. In contrast, Pt/$Ce_xZr_{1-x}O_2$ catalysts at 300 °C must be considered to promote reaction steps 1−3 based on the SSITKA−DRIFTS studies, which indicated that formates and carbonates provided the red isotopic shift (Figure 7b−c). According to reaction steps 2 and 3, carbonates contribute to the reduction of the support. It was reported[36] that reaction step 3 is favored in the presence of Pt, which participates in a charge transfer between Pt and O_L at the Pt−support interface, thus reducing the bonding strength in Ce−O−Ce. It is therefore suggested that addition of Zr^{4+} in the ceria lattice promotes reaction step 3 according to the "redox" route.

3.3.3. CO_2 Readsorption Effects. To check the reversibility of reaction step 3 on Pt/$Ce_{0.5}Zr_{0.5}O_2$ at 200 and 300 °C and to explain correctly the observed red isotopic shift associated with carbonate species, SSITKA−MS experiments similar to those presented in Figure 8b have been performed but using different amounts of catalyst sample (10−30 mg diluted in SiO_2) so as to keep the same GHSV (h^{-1}) as that used in the experiment reported in Figure 8b. Linear extrapolation of the concentration (μmol·g_{cat}^{-1}) of "C-pool" to W_{cat} = 0.0 leads to the estimation of "C-pool" free of CO_2 readsorption on nonactive catalytic sites, thus avoiding overestimation of the "C-pool".[13,27] These results are presented in Figure 9, and the corrected values of "C-pool" are those reported in Table 1.

The corrections made to the concentration of "C-pool" due to CO_2 readsorption effects for the Pt/$Ce_xZr_{1-x}O_2$ catalysts were in the range of 3−20%. In contrast, CO_2 readsorption did occur to a greater extent (~70% correction) on Pt/CeO_2.[15] The latter result implies that Pt/$Ce_xZr_{1-x}O_2$ is less prone to an *irreversible* deactivation by CO_2 compared with Pt/CeO_2, and this important finding offers another explanation for the larger WGS activity observed on Pt/$Ce_xZr_{1-x}O_2$ compared with Pt/CeO_2 (Section 3.2).

The proposed "redox" mechanism over the present WGS catalytic system involves the formation of a "*carbonate-type*" intermediate on the support, which eventually leads to CO_2(g) and an oxygen vacant site. This intermediate must be considered as the most populated active reaction intermediate in the "carbon path" of WGS, according to the results reported

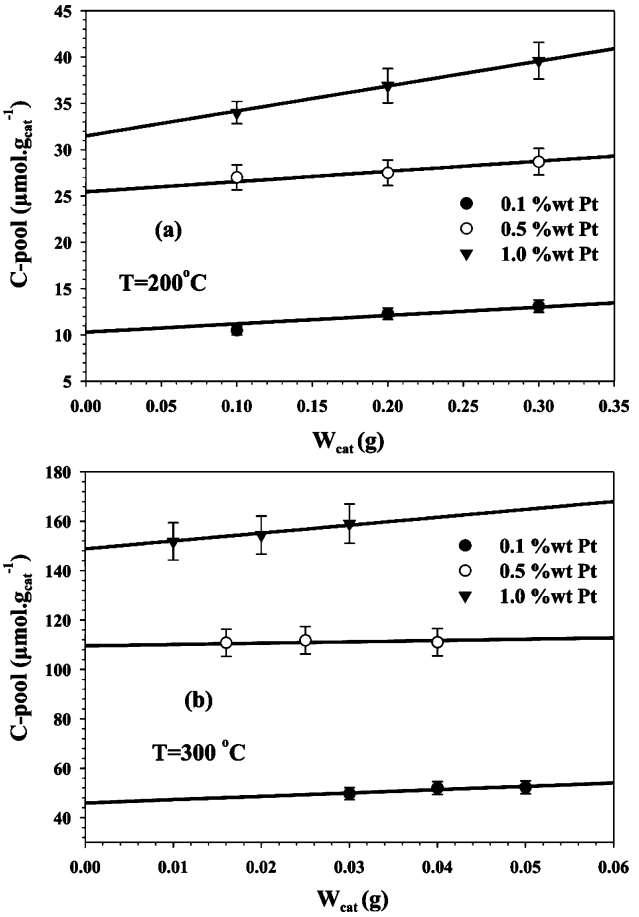

Figure 9. Dependence of the concentration (μmol·g_{cat}^{-1}) of *active* "carbon-containing" ("C-pool") reaction intermediates found in the carbon path of the WGS on x wt % Pt/$Ce_{0.5}Zr_{0.5}O_2$ (x = 0.1, 0.5 and 1.0) catalysts on the amount of catalyst used (W_{cat}, g) in the SSITKA−MS studies at 200 °C (a) and 300 °C (b). Extrapolation of the straight line to W_{cat} = 0 provides the concentration of *active* "C-pool" free of CO_2 readsorption effects.

in Table 1. The reversible chemisorption step of CO_2(g) on an oxygen vacant site according to reaction step 4 cannot be excluded.[96]

$$CO_2(g) + (\square_L)^{n-} \leftrightarrow [CO_2]^{n-} -_L \quad (4)$$

The significance of this step was checked by an isothermal transient "redox" experiment, in which a fresh 1 wt % Pt/$Ce_{0.5}Zr_{0.5}O_2$ catalyst sample after standard pretreatment was exposed to a 2 vol %H_2/He gas mixture at 300 °C. The amount of H_2 consumed or, equivalently, the lattice oxygen removed and, thus, of oxygen vacant sites formed was 25 μmol·g^{-1}. This value is significantly lower than that corresponding to the "C-pool" reported in Table 1 (149 μmol·g^{-1}, reaction step 3). Thus, it is rather clear and convincing that the red isotopic shift observed due to adsorbed carbonates is largely due to reaction step 3 and not to reaction step 4.

3.3.4. "Redox" vs "Associative Formate" WGS Reaction Mechanism. The aim of the transient isotopic experiment described in Section 2.4.3 was to conclude whether the formate species is a major reaction intermediate found in the WGS reaction path on the present 0.5 wt % Pt/$Ce_{0.5}Zr_{0.5}O_2$ catalyst. Figure 10 shows transient response curves of H_2, $^{12}CO_2$, and $^{13}CO_2$ obtained under the 10 vol % H_2O/Ar (300 °C, t) gas

dx.doi.org/10.1021/cs3006204 | ACS Catal. 2012, 2, 2729−2742

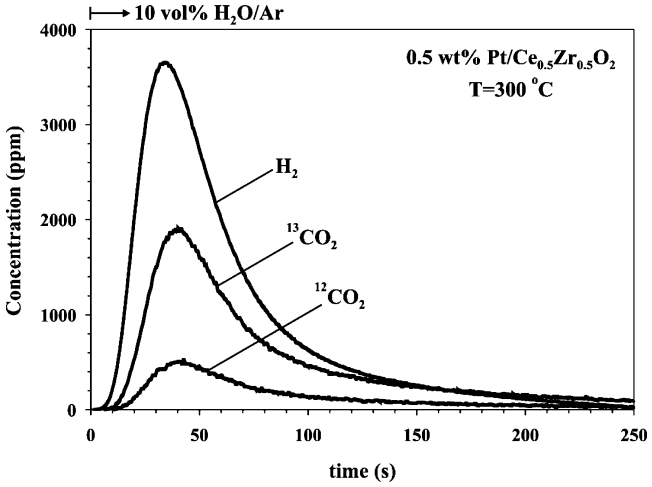

Figure 10. Transient response curves of H_2, $^{12}CO_2$, and $^{13}CO_2$ obtained on the 0.5 wt % $Pt/Ce_{0.5}Zr_{0.5}O_2$ catalyst at 300 °C according to the following gas delivery sequence: 3 vol % ^{12}CO/10 vol % H_2O/Ar (300 °C, 30 min) → 3 vol % ^{13}CO/Ar (300 °C, 5 min) → 10 vol % H_2O/Ar (300 °C, *t*).

treatment of the catalyst according to the gas delivery sequence described in Section 2.4.3. The evolution of $^{13}CO_2(g)$ corresponds to the reaction of adsorbed ^{13}CO-s with water via the elementary reaction steps 2−3 and the following one, reaction 5, which is responsible for the formation of dihydrogen:

$$(O -_L + \square_L)^{n-} + H_2O(g) \leftrightarrow (O -_L + O_L)^{n-} + H_2(g) \quad (5)$$

On the other hand, the evolution of the $^{12}CO_2(g)$ transient response curve corresponds to the reaction of adsorbed $H^{12}COO-$ species with water. The former was formed under the WGS, but its carbonyl could not be exchanged with $^{13}CO(g)$ during the ^{13}CO/Ar gas treatment. It is important to note here that in our previous studies,[14] (i) the extent of decomposition of $H^{12}COO-$ under the ^{13}CO/Ar gas treatment was very small, and (ii) the $^{12}CO_2(g)$ response was not the result of any reaction of irreversibly adsorbed nonactive carbonate species with water upon the H_2O/Ar gas treatment. Integration of the transient response curves of $^{13}CO_2$ and $^{12}CO_2$ provides the concentration of CO_{ads} and $HCOO-$ species, respectively, which were formed under steady-state WGS. These quantities were found to be 33.6 and 10.9 $\mu mol \cdot g^{-1}$ for the $^{13}CO_2(g)$ and $^{12}CO_2(g)$ transient responses, respectively. The amount of H_2 produced was 55.4 $\mu mol \cdot g^{-1}$, which is ∼20% higher than the sum of the quantities of CO_2's according to the stoichiometry of the WGS reaction. The small difference in the material balance that appeared can be justified as due to some readsorption of produced CO_2's on the catalyst surface at 300 °C, as previously discussed.

It is clearly seen in Figure 10 that the initial transient formation rate of $^{13}CO_2$ (t_M = 40 s at peak maximum) is larger by a factor of 3.7 compared with the maximum rate of $^{12}CO_2$ formation. Considering that the surface concentration of adsorbed CO and formate at t_M differ only by a factor of 2.5,[14] it is reasonable to conclude that the rate of CO_2 formation via the "redox" mechanism largely controls the overall WGS reaction rate. This "redox" mechanism is depicted in Scheme 1b. In the case of CeO_2 (Scheme 1a), the "redox" mechanism involves an active adsorbed CO on Pt sites at the

Scheme 1. Proposed "Redox" Mechanism of the Water−Gas Shift Reaction on Pt/CeO_2 (a) and $Pt/Ce_xZr_{1-x}O_2$ (b) Catalysts

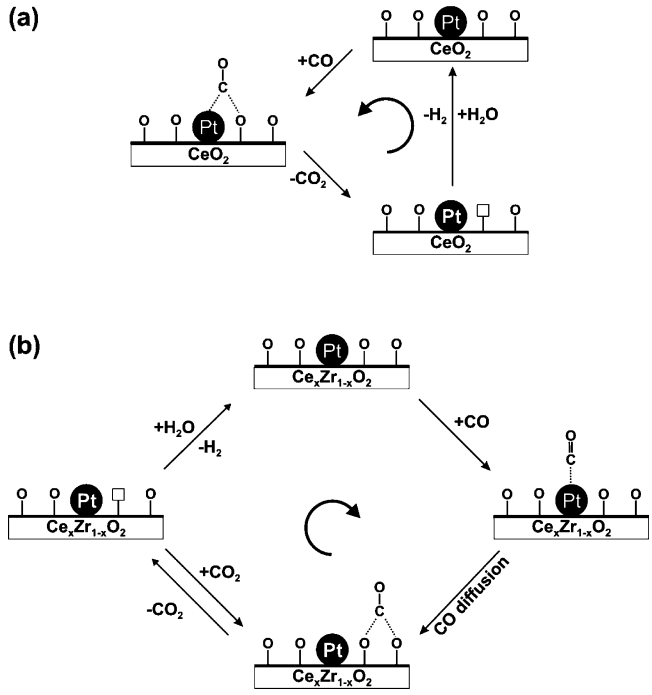

metal−support interface, and an adjacent lattice support oxygen to form $CO_2(g)$. Thus, the introduction of Zr^{4+} into the ceria lattice has changed the chemical structure of the *active* "C-containing" intermediate of the WGS reaction on $Pt/Ce_xZr_{1-x}O_2$ compared wtih Pt/CeO_2.

Although the analysis of data presented in Figure 10 does not estimate individual steady-state rates of the two parallel reaction paths, namely, "redox" and "associative formate", this should be considered as an alternative powerful tool to those proposed earlier,[43,97−99] which allows investigation of the contribution of formate species to the overall WGS reaction rate in a quantitative manner.

CONCLUSIONS

The following conclusions based on the results of the present work can be considered:

(a) The presence of Ce^{3+} sites at the metal−support interface ($Pt-\square_s-Ce^{3+}$) was probed by DRIFTS−CO chemisorption studies. Introduction of Zr^{4+} into the ceria lattice decreases the $Ce^{4+} \rightarrow Ce^{3+}$ reduction energy, thus increasing the concentration of defect Ce^{3+} sites. The latter is associated with the superior WGS catalytic activity exhibited by $Pt/Ce_xZr_{1-x}O_2$ compared with Pt/CeO_2.

(b) The mechanism of the WGS over Pt supported on $Ce_xZr_{1-x}O_2$ (x = 0.3, 0.5, and 0.7) in the 200−300 °C range using 10 vol % H_2O and a H_2O/CO ratio of ∼3.3 was found to depend on reaction temperature. At 200 °C, the "redox" mechanism involves the formation of adsorbed CO and a "carbonate-type" reaction intermediate that leads to $CO_2(g)$ and an oxygen vacant site. The latter intermediate must be considered as the most populated *active* intermediate in the "carbon path" of the WGS reaction. It was proved that only a small part of the

dx.doi.org/10.1021/cs3006204 | ACS Catal. 2012, 2, 2729−2742

CO_2(g) product is reversibly chemisorbed on oxygen vacant sites present in the "carbon path" of the WGS. At 300 °C, the WGS reaction was found to proceed mainly through a "redox" bifunctional mechanism and, to a lesser extent, through a parallel "associative formate with −OH group regeneration" mechanism.[14] The latter mechanism implies the presence of an active formate intermediate according to the SSITKA−DRIFTS studies performed.

(c) The introduction of Zr^{4+} into the ceria lattice has changed the structure of the main active "C-containing" intermediate of the WGS for the Pt/$Ce_xZr_{1-x}O_2$ catalytic system compared with Pt/CeO_2.

(d) The concentration (μmol·g^{-1} or θ (based on Pt_s)) of active "C-containing" (mainly adsorbed CO on Pt and carbonates on the support) and "H-containing" intermediates (mainly OH/H species on the support) formed during the WGS on Pt/$Ce_{0.5}Zr_{0.5}O_2$ was found to strongly depend on the reaction temperature, support chemical composition (Ce/Zr atom ratio), and Pt particle size (or Pt loading). These important kinetic parameters influence the shape of the X_{CO} (%) versus T profile observed.

(e) There is a linear correlation of the specific kinetic rate of WGS (μmol CO.cm^{-1}.s^{-1}) with Pt particle size. This result explains the observed progressive shift of the X_{CO} (%)-vs-T profile toward lower temperatures with increasing Pt loading (or Pt mean particle size) in the 0.1−1.0 wt % range. This result strongly suggests that there is a structure-sensitive nature for the WGS over the present Pt/$Ce_xZr_{1-x}O_2$ catalysts.

■ ASSOCIATED CONTENT

Supporting Information

Catalyst surface texture, bulk chemical composition (Raman studies), Pt particle size distribution and dispersion measurements (HAADF/STEM and H_2-TPDs), H_2-TPR uptakes, and catalytic performance evaluation (X_{CO} vs T) of Pt/$Ce_xZr_{1-x}O_2$ solids. This information is available free of charge via the Internet at http://pubs.acs.org/.

■ AUTHOR INFORMATION

Corresponding Author

*Phone: +357 22 892776. Fax: +357 22 892801. E-mail: efstath@ucy.ac.cy.

Notes

The authors declare no competing financial interest.

■ ACKNOWLEDGMENTS

The European Regional Development Fund, the Republic of Cyprus, and the Research Promotion Foundation of Cyprus are gratefully acknowledged for their financial support through the project PENEK/ENISX/0308/50. We also thank Dr. Sergio García-Rodríguez (ICP/CSIC, Madrid, Spain) for the HAADF/STEM measurements.

■ REFERENCES

(1) Park, E. D.; Lee, D.; Lee, H. C. *Catal. Today* **2009**, *139*, 280−290.
(2) Basagiannis, A. C.; Verykios, X. E. *Appl. Catal., A* **2006**, *308*, 182−193.
(3) Chernik, S.; French, R.; Feik, C.; Chornet, E. *Ind. Eng. Chem. Res.* **2002**, *41*, 4209−4215.
(4) Cortright, R. D.; Davda, R. R.; Dumesic, J. A. *Nature* **2002**, *418*, 964−967.
(5) Fu, Q.; Saltsburg, H.; Flytzani-Stephanopoulos, M. *Science* **2003**, *301*, 935−938 , and references therein..
(6) Jacobs, G.; Davis, B. H. *Catalysis* **2007**, *20*, 122−285.
(7) Farrauto, R.; Hwang, S.; Shore, L.; Ruettinger, W.; Lampert, J.; Giroux, T.; Liu, Y.; Ilinich, O. *Annu. Rev. Mater. Res.* **2003**, *33*, 1−27.
(8) Mhadeshwar, A. B.; Vlachos, D. G. *Catal. Today* **2005**, *105*, 162−172.
(9) Liu, X. S.; Ruettinger, W.; Xu, X. M.; Farrauto, R. *Appl. Catal., B* **2005**, *56*, 69−75.
(10) Wang, X.; Gorte, R. J.; Wagner, J. P. *J. Catal.* **2002**, *212*, 225−230.
(11) Azzam, K. G.; Babich, I. V.; Seshan, K.; Lefferts, L. *J. Catal.* **2007**, *251*, 153−162.
(12) Azzam, K. G.; Babich, I. V.; Seshan, K.; Lefferts, L. *J. Catal.* **2007**, *251*, 163−171.
(13) Ricote, S.; Jacobs, G.; Milling, M.; Ji, Y.; Patterson, P. M.; Davis, B. H. *Appl. Catal., A* **2006**, *303*, 35−47.
(14) Kalamaras, C. M.; Americanou, S.; Efstathiou, A. M. *J. Catal.* **2011**, *279*, 287−300.
(15) Kalamaras, C. M.; González, I. D.; Navarro, R. M.; Fierro, J. L. G.; Efstathiou, A. M. *J. Phys. Chem. C* **2011**, *115*, 11595−11610.
(16) Barrio, L.; Zhou, G.; González, I. D.; Estrella, M.; Hanson, J.; Rodriguez, J. A.; Navarro, R. M.; Fierro, J. L. G. *Phys. Chem. Chem. Phys.* **2012**, *14*, 2192−2202.
(17) Ribeiro, M. C.; Jacobs, G.; Linganiso, L.; Azzam, K. G.; Graham, U. M.; Davis, B. H. *ACS Catal.* **2011**, *1*, 1375−1383.
(18) Lee, H. C.; Lee, D.; Lim, O. Y.; Kim, S.; Kim, Y. T.; Ko, E. Y. *Stud. Surf. Sci. Catal.* **2007**, *167*, 201−206.
(19) Vignatti, C. I.; Avila, M. S.; Apesteguia, C. R.; Garetto, T. F. *Catal. Today* **2011**, *171*, 297−303.
(20) Panagiotopoulou, P.; Papavasiliou, J.; Avgouropoulos, G.; Ioannides, T.; Kondarides, D. I. *Chem. Eng. J.* **2007**, *134*, 16−22.
(21) Kim, Y. T.; You, S. J.; Park, E. D. *Int. J. Hydrogen Energy* **2012**, *37*, 1465−1474.
(22) Ruettinger, W.; Liu, X.; Farrauto, R. *Appl. Catal., B* **2006**, *65*, 135−141.
(23) Radhakrishnan, R.; Willigan, R.; Dardas, Z.; Vanderspurt, T. *AIChE J.* **2006**, *52*, 1888−1894.
(24) Bi, Y.; Xu, H.; Li, W.; Goldbach, A. *Int. J. Hydrogen Energy* **2009**, *34*, 2965−2971.
(25) Burch, R. *Phys. Chem. Chem. Phys.* **2006**, *8*, 5483−5500.
(26) Meunier, F. C. *Catal. Today* **2010**, *155*, 164−171.
(27) Efstathiou, A. M.; Gleaves, J. T.; Yablonsky, G. S. In *Characterization of Solid Materials and Heterogeneous Catalysts*; Che, M., Védrine, J. C., Eds.; Wiley-VCH: Weinheim, 2012; Vol. *2*, pp 1013−1073.
(28) Bunluesin, T.; Gorte, R. J.; Graham, G. W. *Appl. Catal., B* **1998**, *15*, 107−114.
(29) Gorte, R. J.; Zhao, S. *Catal. Today* **2005**, *104*, 18−24.
(30) Hilaire, S.; Wang, X; Luo, T.; Gorte, R. J.; Wagner, J. *Appl. Catal., A* **2001**, *215*, 271−278.
(31) Li, Y.; Fu, Q.; Flytzani-Stephanopoulos, M. *Appl. Catal., B* **2000**, *27*, 179−191.
(32) Liu, W.; Flytzani-Stephanopoulos, M. *J. Catal.* **1995**, *153*, 317−332.
(33) Silberova, B. A. A.; Mul, G.; Makkee, M. M.; Moulijn, J. A. *J. Catal.* **2006**, *243*, 171−182.
(34) Kalamaras, C. M.; Panagiotopoulou, P.; Kondarides, D. I.; Efstathiou, A. M. *J. Catal.* **2009**, *264*, 117−129.
(35) Chenu, E.; Jacobs, G.; Crawford, A. C.; Keogh, R. A.; Patterson, P. M.; Sparks, D. E.; Davis, B. H. *Appl. Catal., B* **2005**, *59*, 45−58.
(36) Jacobs, G.; Graham, U. M.; Chenu, E.; Patterson, P. M.; Dozier, A.; Davis, B. H. *J. Catal.* **2005**, *229*, 499−512.
(37) Jacobs, G.; Williams, L; Graham, U.; Sparks, D.; Davis, B. H. *J. Phys. Chem. B* **2003**, *107*, 10398−10404.
(38) Jacobs, G.; Williams, L.; Graham, U.; Thomas, G. A.; Sparks, D. E.; Davis, B. H. *Appl. Catal., A* **2003**, *252*, 107−118.

(39) Shido, T.; Iwasawa, Y. *J. Catal.* **1993**, *141*, 71−81.
(40) Duprez, D. *Catal. Today* **2006**, *112*, 17−22.
(41) Jacobs, G.; Crawford, A. C.; Davis, B. H. *Catal. Lett.* **2005**, *100*, 147−152.
(42) Meunier, F. C.; Goguet, A.; Hardacre, C.; Burch, R.; Thompsett, D. *J. Catal.* **2007**, *252*, 18−22.
(43) Meunier, F. C.; Reid, D.; Goguey, A.; Shekhtman, S.; Hardacre, C.; Burch, R.; Deng, W.; Stephanopoulos, M. F. *J. Catal.* **2007**, *247*, 277−287.
(44) Stamatakis, M.; Chen, Y.; Vlachos, D. G. *J. Phys. Chem. C* **2011**, *115*, 24750−24762.
(45) Costa, C. N.; Anastasiadou, T.; Efstathiou, A. M. *J. Catal.* **2000**, *194*, 250−265.
(46) Costa, C. N.; Efstathiou, A. M. *J. Phys. Chem. B* **2004**, *108*, 2620−2630.
(47) Smith, B. C. *Fundamentals of Fourier Transform Infrared Spectroscopy*; CRC Press; Boca Raton, FL, 1996.
(48) Polychronopoulou, K.; Costa, C. N.; Efstathiou, A. M. *Appl. Catal., A* **2004**, *272*, 37−52.
(49) Kalamaras, C. M.; Olympiou, G. G.; Efstathiou, A. M. *Catal. Today* **2008**, *138*, 228−234.
(50) Sirita, J.; Phanichphant, S.; Meunier, F. C. *Anal. Chem.* **2007**, *79*, 3912−3918.
(51) Efstathiou, A. M.; Verykios, X. E. *Appl. Catal., A* **1997**, *151*, 109−166.
(52) Olympiou, G. G.; Kalamaras, C. M.; Zeinalipour-Yazdi, C. D.; Efstathiou, A. M. *Catal. Today* **2007**, *127*, 304−318.
(53) Wang, X.; Lu, G.; Guo, Y.; Xue, Y.; Jiang, L.; Guo, Y.; Zhang, Z. *Catal. Today* **2007**, *126*, 412−419.
(54) Youn, M. Y.; Seo, J. G.; Cho, K. M.; Park, S.; Park, D. R.; Jung, J. C.; Song, I. K. *Int. J. Hydrogen Energy* **2008**, *33*, 5052−5059.
(55) Yashima, M.; Morimoto, K.; Ishizawa, N.; Yoshimura, M. *J. Am. Ceram. Soc.* **1993**, *76*, 1745−1750.
(56) Hori, C. E.; Permana, H.; Ng, K. Y. S.; Brenner, A.; More, K.; Rahmoeller, K. M.; Belton, D. *Appl. Catal., B* **1998**, *16*, 105−117.
(57) Rossignol, S.; Madier, Y.; Duprez, D. *Catal. Today* **1999**, *50*, 261−270.
(58) Janvier, C.; Pijolat, M.; Valdivieso, F.; Soustelle, M.; Zing, C. *J. Eur. Ceram. Soc.* **1998**, *18*, 1331−1337.
(59) Anderson, J. R.; Pratt, K. C. *Introduction to Characterization and Testing of Catalysts*; Academic Press: New York, 1985.
(60) Barth, R.; Pitchai, R.; Anderson, L. R.; Verykios, X. E. *J. Catal.* **1989**, *116*, 61−71.
(61) Bourane, A.; Dulaurent, O.; Bianchi, D. *J. Catal.* **2000**, *196*, 115−125.
(62) Cant, N. W.; Donaldson, R. A. *J. Catal.* **1981**, *71*, 320−330.
(63) Haalant, D. M.; Williams, F. L. *J. Catal.* **1982**, *110*, 319−329.
(64) Li, Y. E.; Boeeker, D.; Gonzalez, R. D. *J. Catal.* **1988**, *110*, 319−329.
(65) Pozdnyakova, O.; Teschner, D.; Wootsch, A.; Krohnert, J.; Steinhauer, B.; Sauer, H.; Toth, L.; Jentoft, F. C.; Gericke, A. K.; Paal, Z.; Schlogl, R. *J. Catal.* **2006**, *237*, 1−16.
(66) Primet, M.; Basset, J. M.; Mathieu, M. V.; Prettre, M. *J. Catal.* **1973**, *29*, 213−223.
(67) Rasko, J. *J. Catal.* **2003**, *217*, 478−486.
(68) Tellinger, O. P.; Teschner, D.; Krohnert, J.; Jentoft, F. C.; Gericke, A. K.; Schlogl, R.; Wootsch, A. *J. Phys. Chem. C* **2007**, *111*, 5426−5431.
(69) Tibiletti, D.; Goguet, A.; Reid, D.; Meunier, F. C.; Burch, R. *Catal. Today* **2006**, *113*, 94−101.
(70) Yeung, C. M. Y.; Meunier, F.; Burch, R.; Thompsett, D.; Tsang, S. C. *J. Phys. Chem. B* **2006**, *110*, 8540−8543.
(71) Yee, A.; Morrison, S. J.; Idriss, H. *J. Catal.* **2000**, *191*, 30−45.
(72) Primet, M. *J. Catal.* **1984**, *88*, 273−282.
(73) Zhu, H.; Qin, Z.; Shan, W.; Shen, W.; Wang, J. *J. Catal.* **2004**, *225*, 267−277.
(74) Jacobs, G.; Davis, B. H. *Appl. Catal., A* **2007**, *333*, 192−201.
(75) Balducci, G.; Kaspar, J.; Fornasiero, P.; Graziani, M.; Islam, M. S. *J. Phys. Chem. B* **1998**, *102*, 557−561.
(76) Fu, Q.; Deng, W.; Saltsburg, H.; Flytzani-Stephanopoulos, M. *Appl. Catal., B* **2005**, *56*, 57−68.
(77) Balakos, M. W.; Madden, M. R.; Walsh, T. L.; Wagner, J. P. *Proceedings of the AIChE Spring National Meeting*; New Orleans, LA, 2004.
(78) Alexeev, O. S.; Chin, S. Y.; Engelhard, M. H.; Ortiz-Soto, L.; Amiridis, M. D. *J. Phys. Chem. B* **2005**, *109*, 23430.
(79) Jacobs, G.; Patterson, P. M.; Williams, L.; Chenu, E.; Sparks, D.; Thomas, G.; Davis, B. H. *Appl. Catal., A* **2004**, *262*, 177−187.
(80) Little, L. H. *IR Spectra of Adsorbed Species*; Academic Press: New York, 1966.
(81) Panagiotopoulou, P.; Kondarides, D. I. *J. Catal.* **2008**, *260*, 141−149.
(82) Jacobs, G.; Patterson, P. M.; Graham, U. M.; Crawford, A. C.; Davis, B. H. *Int. J. Hydrogen Energy* **2005**, *30*, 1265−1276.
(83) Jacobs, G.; Ricote, S.; Davis, B. H. *Appl. Catal., A* **2005**, *284*, 31−38.
(84) Jacobs, G.; Ricote, S.; Davis, B. H. *Appl. Catal., A* **2006**, *302*, 14−21.
(85) Jacobs, G.; Patterson, P. M.; Graham, U. M.; Sparks, D. E.; Davis, B. H. *Appl. Catal., A* **2004**, *269*, 63−73.
(86) Li, C.; Sakata, Y.; Arai, T.; Domen, K.; Maruya, K.-i.; Onishi, T. *J. Chem. Soc. Faraday Trans. 1* **1989**, *85*, 929−943.
(87) Li, C.; Sakata, Y.; Arai, T.; Domen, K.; Maruya, K.; Onishi, T. *J. Chem. Soc. Faraday Trans. 1* **1989**, *85*, 1451−1455.
(88) Martin, D.; Duprez, D. *J. Phys. Chem. B* **1997**, *101*, 4428−4436.
(89) Meunier, F. C.; Tibiletti, D.; Goguet, A.; Burch, R. *Oil Gas Sci. Technol.* **2006**, *61*, 497−502.
(90) Meunier, F. C.; Tibiletti, D.; Goguet, A.; Shekhtman, S.; Hardacre, C.; Burch, R. *Catal. Today* **2007**, *126*, 143−147.
(91) Menetrey, M.; Markovits, A.; Minot, C. *Surf. Sci.* **2003**, *524*, 49−62.
(92) Leppelt, R.; Schumacher, B.; Plzak, V.; Kinne, M.; Behm, R. J. *J. Catal.* **2006**, *244*, 137−152.
(93) Panagiotopoulou, P.; Christodoulakis, A.; Kondarides, D. I.; Boghosian, S. *J. Catal.* **2006**, *240*, 114−125.
(94) Jacobs, G.; Crawford, A.; Williams, L.; Patterson, P. M.; Davis, B. H. *Appl. Catal., A* **2004**, *267*, 27−33.
(95) Shido, T.; Iwasawa, Y. *J. Catal.* **1992**, *136*, 493−503.
(96) Tejuca, L. G.; Bell, A. T.; Fierro, J. L. G.; Peña, M. A. *Appl. Surf. Sci.* **1988**, *31*, 301−316.
(97) Bravo-Suárez, J. J.; Bando, K. K.; Lu, J.; Haruta, M.; Fujitani, T.; Oyama, S. T. *J. Phys. Chem. C* **2008**, *112*, 1115−1123.
(98) Gott, T.; Oyama, S. T. *J. Catal.* **2009**, *263*, 359−371.
(99) Reed, C.; Xi, Y.; Oyama, S. T. *J. Catal.* **2005**, *235*, 378−392.